UNIVERSITY OF CALIFORNIA
Los Angeles

Fluid Dynamics of an Electrowetting Drop: Theories, Simulations, and Experiments

A dissertation submitted in partial satisfaction
of the requirements for the degree
Doctor of Philosophy in Mechanical Engineering

by

Hsiang-Wei Lu

2007

The dissertation of Hsiang-Wei Lu is approved.

Chih-Ming Ho

Pirouz Kavehpour

Andrea L. Bertozzi, Committee Co-chair

Chang-Jin Kim, Committee Co-chair

University of California, Los Angeles

2007

To Baochi, my parents, Emily and Grace.

Table of Contents

List of Figures

List of Tables

ACKNOWLEDGMENTS

First of all I would like to thank Professors Andrea Bertozzi and Chang-Jin "CJ" Kim, my advisors, who gave me invaluable advises and encouragements on conducting sound research. The micro-PIV experimental study would not be possible without the support of Professor Carl Meinhart. Many thanks to Professor Karl Glasner for the assistance in developing the diffuse interface model. Professors Pirouz Kavehpour, and Anette Hosoi provided many invaluable discussions on fluid dynamics. The work would not have been possible without the support of my wife and my parents. Thanks also go to the members of Micromanufacturing Lab, who filled many difficult hours with fun memories. Their dedications to research constitute a significant part of my inspiration. I would also like to thank Hamarz Aryafar, Frederic Bottausci, and Kevin Lu in providing invaluable experimental supports. The research of this Ph.D. work has been funded by ONR grant N000140710431, NSF grant ACI-0321917, NASA through Institute for Cell Mimetic for Space Exploration (CMISE), and NIH through Pacific Southwest Regional Center of Excellence.

VITA

1974	Born, Taipei, Taiwan.
1997	B.S. (Aerospace Engineering), University of Maryland, College Park
1999	M.S. (Aeronautics and Astronautics), Massachisetts Institute of Technology
2000–2002	Software engineer, MaK Technologies Designed collision avoidance controller for a Helicopter simulator
2007	Teaching Assistant, Mathematics Department, UCLA. Taught sections of Math 266C (Applied Partial Differential Equations) under direction of Professor Andrea Bertozzi.
2003-present	In MEMS Ph.D. program (Mechanical Engineering)

PUBLICATIONS

H.-W. Lu, K. Glasner, A. L. Bertozzi, and C.-J. Kim. *Electrowetting in a Hele-Shaw Cell.* J. Fluid Mech. **590**:411-435, 2007.

H.-W. Lu, F. Berttousci, C. D. Meinhart, and C.-J. Kim. *Three-Dimensional in EWOD-Driven Droplets by PIV Investigation.* IEEE Conf. MEMS, Tucson, AZ January 2008. (*to appear*).

ABSTRACT OF THE DISSERTATION

Fluid Dynamics of an Electrowetting Drop: Theories, Simulations, and Experiments

by

Hsiang-Wei Lu

Doctor of Philosophy in Mechanical Engineering

University of California, Los Angeles, 2007

Professor Chang-Jin Kim, Co-chair

Professor Andrea L. Bertozzi, Co-chair

Electrowetting has recently been explored as a mechanism for moving small amounts of fluids in typical confined spaces. We propose a diffuse interface model for drop motion, due to electrowetting, in a Hele-Shaw geometry. In the limit of small interface thickness, asymptotic analysis shows the model is equivalent to Hele-Shaw flow with a voltage-modified Young-Laplace boundary condition on the free surface. We show that details of the contact angle significantly affect the timescale of motion in the model. We measure receding and advancing contact angles in the experiments and derive their influences through a reduced order model. These measurements suggest a range of timescales in the Hele-Shaw model which include those observed in the experiment. The shape dynamics and topology changes in the model agree well with the experiment, down to the length scale of the diffuse interface thickness.

In the limit of a thick drop actuated by electrowetting, we experimentally characterize the fluid dynamics by micro particle image velocimetry (micro-PIV). Using the continuity equation, we reconstruct the 3D velocity field from the 2D PIV exper-

imental data. We present some fundamental findings and build valuable insights that will help to design new sophisticated electrowetting microfluidic devices. It is shown that a reversible movement pattern is inefficient for mixing. Efficient mixing must be achieved through designing a irreversible movement pattern that breaks the symmetry of the circulating flow in the electrowetting drop. All the experiments in this dissertation have been performed in a parallel plate device configuration and run by electrowetting-on-dielectric (EWOD).

CHAPTER 1

Introduction

1.1 Electrowetting

The use of capillarity as an actuation mechanism for microdevice has received serious attention because of its dominance in microscale [Kim99]. Various microfluidic actuators utilizing the surface tension are reviewed by Darhuber and Troian [DT05]. Due to the simple chip fabrication, ease of electronic control, and low power consumption, electrowetting, especially electrowetting-on-dielectric (EWOD) has become a popular mechanism for microfluidic actuations. The theory of electrowetting and its initial applications are well reviewed in literatures [MB05, Fai07, MK07]. Lippmann first studied electrocapillary in the context of a mercury-electrolyte interface. The electric double layer is treated as a parallel plate capacitor [Lip75],

$$\gamma_{sl}(V) = \gamma_{sl}(0) - \frac{1}{2}cV^2, \tag{1.1}$$

where γ_{sl} is the solid-liquid interfacial energy, c is the capacitance per area of the electric double layer, and V is the voltage across the double layer. The potential energy stored in the capacitor is expended toward lowering the surface energy. A locally applied voltage then creates the surface energy variation to induce drop motion. While equation 1.1 is usually derived from thermodynamic energy approach, it has also been recovered by Kang [Kan02] through calculation of the electro-hydrodynamic forces on a conducting liquid wedge on a perfect dielectric.

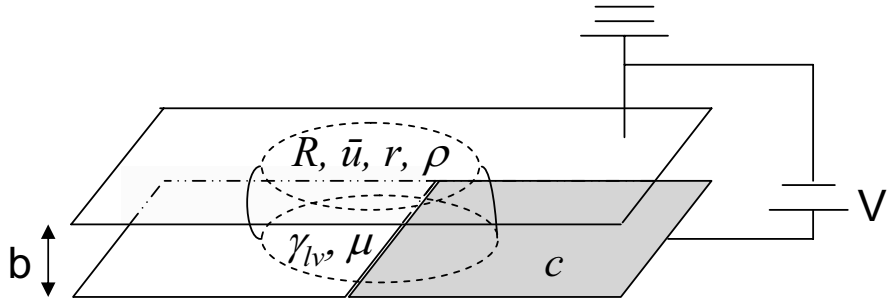

Figure 1.1: Illustration of the electrowetting device.

The electrowetting device we consider has a parallel-plate configuration as shown in figure 1.1. The fabrication and the experimental details will be given in the following section. It consists of a fluid drop constrained between two solid substrates separated by a distance, b. Dielectric breakdown across the electric double layer limits the applicable voltage. Depositing a thin dielectric film ($\sim 0.1\mu m$) using microfabrication techniques common in micro electromechanical systems (MEMS) prevents such breakdown without incurring significant voltage penalty[MCG02], making electrowetting on dielectric (EWOD) a practical mechanism of micro-scale drop manipulation. For such configuration, c in (1.1) represents the capacitance per area of the dielectric. Lee and Kim [LK98] demonstrated the first working micro device driven by electrically controlled surface tension with mercury drop in water. Handling of discrete water drops in air soon followed [Kim00, LMF01, LMF02]. Currently, microfluidic chips capable of cutting, merging, and transport of drops by electrowetting in Hele-Shaw cell geometry was demonstrated in air by Cho et al. [CMF01] and mostly in oil by Pollack et al. [PFS00]. In addition, Hayes and Feenstra utilized a similar principle to produce a video speed display device [HF03].

Despite its popularity, fundamental understanding of the fluid dynamics inside of drops actuated by electrowetting remains limited. The electrode shape, the magnitude

and the duration of the applied voltage all have an influence on the transport processes in the electrowetting drops. A quantitative model that relates these design variables to the fluid dynamics will help design sophisticated electrowetting devices in the future.

1.2 Dimensional analysis

We first perform a dimensional analysis to understand the different physical forces involved in the fluid dynamics of a drop actuated by electrowetting. There are six physical variables associated with a fluid drop constrained from the top and bottom by a parallel plate electrowetting device as show in figure 1.1. The drop has a disc radius, R, and is moving at a typical velocity $\bar{u}$. The fluid has mechanical properties of density, ρ, surface tension, γ_{lv}, and dynamic viscosity, μ. In the electrostatic limit, an important electrical properties is the resistivity, r, of the fluid. The electrowetting device is formed of two plates separated by the height, b, with constant potential difference, V, between them. The capacitance per area of the thin dielectric film on the bottom plate is c. The system is described by a total of nine physical variables using the fundamental units of length, mass, time, and charge. Dimensional analysis gives five independent dimensionless quantities that parameterize the fluid dynamics in the fluid drop. These quantities typically represents the ratios of different physical forces. We can glimpse into the different forces and their importance by study the forms and the magnitudes of the dimensionless quantities.

The first quantity is the Reynolds number, $Re = \rho\bar{u}R/\mu$, which represents the ratio of inertia over viscosity. Since we are moving the drop by changing the surface energy, another important quantity is the capillary number, $Ca = \mu\bar{u}/\gamma_{lv}$, which represents the viscosity over the surface tension. The electrowetting number, $\omega = cV^2/\gamma_{lv}$, represents the ratio of the electrostatic energy stored across the dielectric film over the surface tension [SMG03]. In the electrostatic limit, the charging time of the capacitor across

the dielectric film is bcr. The ratio of the charging time over the timescale of fluid convection, $R/\bar{u}$, gives us another quantity, $\bar{u}bcr/R$. As we will show in chapter 2, the small value of this quantity allows us to make a quasi-static model of electrowetting on a moving drop. The last but an important geometric quantity is the aspect ratio of the drop, $\alpha = b/R$, which can be interpreted as the ratio of the liquid-vapor surface area over the liquid-solid surface area.

Dimensional analysis allows us to reduce the number of variables for the problem. However, the functional relationships between the dimensionless quantities must be determined in the experimental and theoretical studies of the physics. As we will see in chapter 3, the aspect ratio of the drop is a parameter that further modifies other dimensionless quantities. When the drop geometry approaches that of a Hele-Shaw cell i.e, $\alpha \to 0$, the fluid dynamics can be simplified tremendously.

1.3 Hele-Shaw cell

Significant portion of this work will focus on the fluid dynamics in the electrowetting drops where the drop radius R is much greater than the drop height b, i.e, $\alpha \ll 1$. This drop geometry approximates a Hele-Shaw cell [Hel98], which enjoys a rich history in fluid mechanics [Saf86, Hom87, BKL86, How92, Tan00].

Saffman and Taylor [ST59] first considered a bubble with zero surface tension and found two families of bubble shapes parameterized by the bubble velocity and area. Solving the equations including small surface tension reveals multiple branches of bubble shapes parameterized by relative drop size, aspect ratio, and capillary number [Tan86, Tan87, TS87].

Despite the extensive theoretical investigation, experimental validation of the bubble shapes and velocities has been difficult due to the sensitivity to the conditions at

the bubble/drop interface. For pressure driven flow in a horizontal cell, Kopfsill and Homsy [KH88] observed a variety of unusual bubble shapes. In addition, they found nearly circular bubbles travelling at a velocity nearly an order of magnitude slower than the theoretical prediction. Tanveer and Saffman [TS89] qualitatively attributed the disagreement to perturbations of boundary conditions due to contact angle hysteresis. Park et al. [PMY94] suggests the velocity disagreement and the unusual shapes may be due to surface-active contaminants.

In many of these studies, the pressure jump at the interface was determined from balancing the surface tension against the local hydrodynamic pressure. However, the local hydrodynamic pressure is indirectly controlled through the upstream flow rates. Electrowetting provides a unique way to directly vary the pressure on the free boundary. Knowledge of the electrowetting drop may provide a direct means to investigate the correct boundary condition for the multiphase fluid dynamics in a Hele-Shaw cell.

1.4 Contact line dynamics

Electrowetting devices operates on partially wetting fluid drops that are effected by additional microscopic physics of the surface at the contact line[deG85]. Experimental studies of silicon oil and water displacing air in Hele-Shaw cell have shown that small surface defects strongly impedes the advance of fluid interfaces [PFL95, PF97]. Ortin et al. [CSO99, CSO00] found the fingering instability and the displacement speed of an expanding fluid annulus in a rotating Hele-Shaw cell is highly sensitive to the wetting condition of the outer interface.

The continuum description of the fluid mechanics breaks down near the contact line, resulting in an infinite amount of energy dissipation at the contact line [HS71, Dus79]. Many theoretical studies investigated the contact line dynamics by augment-

ing the continuum mechanics by various mechanisms [Ber93]. They include models based on Navier slip [Gre78, Hoc77], precursor film [deG85, DKB00] and atomistic models [Fre03, Had99]. Inclusion of van der Waal potential in the diffuse interface model was proposed as a regularization of a slowly moving contact line of a partially wetting fluid [Pom02, PP04]. These studies focus on identifying the physical mechanism that allow the motion of a contact line with a single value of contact angle. For moving drops in electrowetting devices, the contact lines are closed curves with each segment moving with a different normal velocity from other segments. Therefore, the contact angles varies along the contact lines. A closely related study by Weinstein et al. [WDU90] investigated the influence of dynamic contact angles on the steady state solutions of viscous fingering in a Hele-Shaw cell. The dynamic contact angle is incorporated into the pressure boundary condition but has only geometric dependence on the steady finger shape. The analysis is special for a travelling wave solution and does not directly carry over to the general flow problem in Hele-Shaw cell.

1.5 Numerical methods

Due to the intense interest in the Hele-Shaw problems, the last ten years have also seen a development of numerical methods for solving the Hele-Shaw problem. The boundary integral method developed by Hou et al. [HLS94] has been quite successful in simulating the long time evolution of free boundary fluid problems in a Hele-Shaw cell. However, simulating drops that undergo topological changes remains a complicated, if not ad hoc, process for methods based on sharp interfaces. Diffuse interface models provide alternative descriptions by defining a phase field variable that assumes a distinct constant value in each bulk phase. The material interface is considered as a region of finite width in which the phase field variable varies rapidly but smoothly from one phase value to another. Such diffuse interface methods naturally handle

topology changes. As we demonstrate in this work, an energy construction provides a convenient framework in which to incorporate a spatially varying surface energy due to electrowetting. Matched asymptotic expansions may be used to demonstrate the equivalence between the diffuse interface dynamics and the sharp interface dynamics in the Hele-Shaw cell.

We develop a diffuse interface framework for the study of Hele-Shaw cell drops that undergo topological changes by electrowetting. Using level set methods, Walker and Shapiro [WS06] considered the unsteady problem of drop deformed by a rapidly changing potential distribution. We consider a viscous flow induced by a steady potential. The related work by Lee et al. [LLG02] considered a diffuse interface in the absence of electrowetting in a Hele-Shaw cell under the influence of gravity. They used a diffuse interface model for the chemical composition, coupled to a classical fluid dynamic equation. Our model describes both the fluid dynamics and the interfacial dynamics through a nonlinear Cahn-Hilliard equation of one phase field variable. Our approach expands on the work done by Glasner [Gla03] and is closely related to that by Kohn and Otto [KO97] and Otto [Ott98].

The result of the diffuse interface model is a fourth order nonlinear partial differential equation (PDE). Such equation places very stiff stability constrains on an explicit numerical scheme. Numerical methods for solving the nonlinear Cahn-Hilliard equation are an active area of research. Barrett et al. [BBG99] proposed a finite element scheme to solve the fourth order equation with degenerate mobility. In addition, the development of numerical methods for solving thin film equations [ZB00, GR00, WB03] are also applicable to the Cahn-Hilliard equation. We study the numerical properties of a biharmonic modified forward time-stepping scheme on different fourth order PDEs. This scheme allows us to efficiently simulate the nonlinear Cahn-Hilliard equation that describes the electrowetting drop motion.

1.6 Three-dimensional effects

While the Hele-Shaw model offers significant physical insights into the fluid dynamics of electrowetting drops, evaporation, cutting and merging operations by electrowetting may invalidate the geometric assumptions made by the model by changing the drop radius significantly. When the radius decreases, details at the air/liquid interface such as fluid recirculation, and surface tension become significant, since the ratio of the air/liquid interfacial area to the solid/liquid interfacial area increases. It is necessary to investigate the dynamics away from the Hele-Shaw limit. We utilize micro particle image velocimetry (micro-PIV) [DSW03] to characterize the microfluidic flow inside of a small drop with $b/R \sim 1$. Micro-PIV measures the two dimensional velocity field in a horizontal x-y plane across the drop at a constant depth, z. By measuring the two dimensional velocity field across different depths, we can reconstruct the velocity component in the third dimension using the continuity equation.

Chapter 2 describes the experimental setup of drop manipulation using electrowetting-on-dielectric (EWOD). Chapter 3 describes the sharp interface fluidic model for the electrowetting drop in Hele-Shaw cell. We also briefly discuss the role of the contact line in the context of the sharp interface model. In chapter 4, we describe the diffuse interface model of the problem. Equivalence with the sharp interface model will be made through matched asymptotic expansions. Chapter 5 details the numerical techniques to simulate the diffused interface model. Comparisons will be made in chapter 6 between the experimental data and the numerical results. To relate the theoretical prediction to the experimental observation, we construct a reduced order model in chapter 7 with constant contact angles similar to the contact angle models discussed in [Saf86]. Chapter 8 details the experimental study on a thick drop using micro-PIV. Finally we will present conclusions and some potential future research topics in chapter 9.

CHAPTER 2

Experimental setup

2.1 Device preparation and experimental procedures

The fabrication of electrowetting devices is documented in a previous study [CMK03]. The devices are fabricated in the UCLA Nanoelectronic Research Facility. The electrowetting devices are fabricated on Schott Borofloat glass wafers (Precision Glass and Optics, Santa Ana, CA) with 4 inches diameter at 0.7 mm thickness. Blanket layers of 100 Å chromium (Cr), and 1000 Å gold (Au) are deposited onto the wafer by a CHA Mark 40 e-beam evaporator (CHA Industries, Fremont, CA). A layer of AZ-5214 photoresist (MicroChemicals, Germany) is spin coated onto the wafer. An etch mask that defines the electrodes, electrical connections, and contact pads are patterned lithographically by an exposure of UV light. The unprotected metal layers are etched off by gold etchant (Transene, Danvers, MA) and chromium etchant (Cyantek, Fremont, CA). A 5000 Å blanket layer of silicon oxide is deposited by PECVD using PlasmaTherm 790 (Unaxis USA, St. Petersburg, FL). The same lithographic procedure is applied to pattern an etch mask for the openings to the contact pads. The silicon oxide covering the contact pads are removed by buffered oxide etchant. A final coating of Cytop fluoropolymer (Asahi Glass, Japan) is deposited by spin coating a 6% solvated solution on the wafer with tapes protecting the contact pads. 2 hours of annealing at 210° Celsius removes the solvent, resulting a polymer layer of $\approx$ 2400 Å in thickness. The top substrate of the electrowetting device is a cleaved glass wafer with a 2000 Å

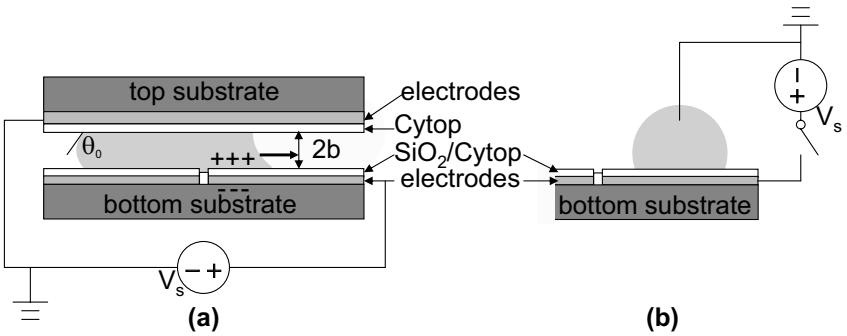

Figure 2.1: (a) Cross-section of the electrowetting device. (b) Experimental setup for static contact angle measurement.

thick conductive coating of indium-tin oxide (ITO). Spin coating a 3% solvated solution followed by annealing gives a thin Cytop layer ($\approx$ 500 Å) on the top substrate. All fluoropolymer layers are applied and annealed just before the experiments to ensure quality of the thin film.

Comparing with the previous work, we enlarge the device geometry by a factor of 10 and use a more viscous fluid such as glycerine to maintain the same Reynolds number as in the smaller devices. Each of the square metal electrodes is 1 cm on a side. This modification allows us to precisely maintain the substrate separation and to directly measure the contact angles. In summery, two dielectric layers are placed on top of the electrodes, a layer of Cytop fluoropolymer (Asahi Glass, Japan) on top of a layer of silicon oxide. A very thin layer of Cytop fluoropolymer then covers the ITO on the top substrate. The thicknesses of the materials used in the device are listed in table 2.1. A drop of fluid with $b/R \sim 0.1$ is dispensed on the bottom substrate. Two solid spacers maintain the substrate separation at 530 μm (see figure 2.1a).

If the top substrate is the same as the bottom substrate, the potential drop across its dielectric layers will involve the electrical properties of the fluid [Fan03]. To simplify the problem, we intentionally use only a thin Cytop film on the top substrate. It is well

Table 2.1: Material thicknesses and dielectric constants of an electrowetting device.

material	thickness	dielectric constant
separation height	529 ± 2 μm	n/a
silicon oxide	498.4 ± 15.5 nm	3.8
fluoropolymer(bottom)	245.8 ± 15.5 nm	2.0
fluoropolymer(top)	50 nm	2.0

know that a thin fluoropolymer film is a poor insulator [SH01] so it only affects the charging time across the thick dielectric layers on the bottom substrate. We conduct a set of static experiments using deionized water with surface tension of 72 dyne/cm to confirm this. First, the capacitance per area of the silicon oxide/Cytop layers on the bottom substrate is characterized by measuring the static contact angle of a sessile drop of deionized water at various static electrical potential (see figure 2.1b). Then we cover the drop with the top substrate and repeat the experiment to characterize the electrowetting effect across the thin Cytop film on the top substrate.

The dynamic experiments uses a glycerine-water mixture with viscosity of 0.020 Pa·s and surface tension of 67 dyne/cm. The half height of the cell is an order of magnitude smaller than the capillary length, $\sqrt{\gamma/\rho g} \approx 2600$ μm, preserving the dominance of surface tension over the gravity. To move a drop, part of the drop interface must extend over an adjacent electrode. The top substrate and the electrode below the drop are grounded. Applying a potential on an adjacent electrode moves the drop to that electrode. The voltage level is varied between 30 V DC and 80 V DC. At each voltage level, we move a drop back and forth between two electrodes ten times by alternately applying the voltage and ground to each electrode. A drop can be split by applying potentials on both sides of the drop. A camera is used to record the motion, from above,

at 30 frames per second. Side views of the menisci at the nose and the tail of a translating drop are recorded at 512×256 resolution by a high speed camera (Vision Research Inc., Wayne, NJ) at 2100 frames per second. The slope of the top substrate is known a priori by focusing on its cleaved edge. The bottom substrate is assumed to have the same slope. Both surfaces create reflections of the menisci allowing us to locate the contact lines. The images are processed by Adobe Photoshop ® and MATLAB ® for edge detection. The capillary numbers of the advancing and receding contact lines are obtained from the side view and the top view of the drop. Time indexed images of the translating and splitting drop are compared against the simulation contours in chapter 6.

2.2 Statics measurements

Using Young's equation, we relate the change of contact angle to the electrowetting voltage,

$$\cos\theta_V - \cos\theta_0 = \frac{cV^2}{2\gamma_{lv}}, \tag{2.1}$$

where θ_V is the static contact angle when we apply a potential, V, on the electrodes. θ_0 is the contact angle at zero potential, and γ_{lv} is the liquid vapor surface tension. Figure 2.2 shows that $\cos\theta_V$ linearly increases as a function of V^2, below a critical voltage. Above the critical voltage, the contact angle saturates and even decreases. This behavior is discussed by previous studies [VP99, PQR00, SH01, VVB99, SMG03]. The model developed in this work will focus on the voltage level below this saturation. The capacitance per area of the silicon oxide/Cytop layers $c = 3.6 \times 10^{-5}$ F is obtained from multiplying the slope of the linear region with $2\gamma_{lv}$. Estimating this quantity by considering the dielectric layers as two capacitors connected in series [MCG02] gives a value close to that measured experimentally. Figure 2.3 shows the static contact angles of

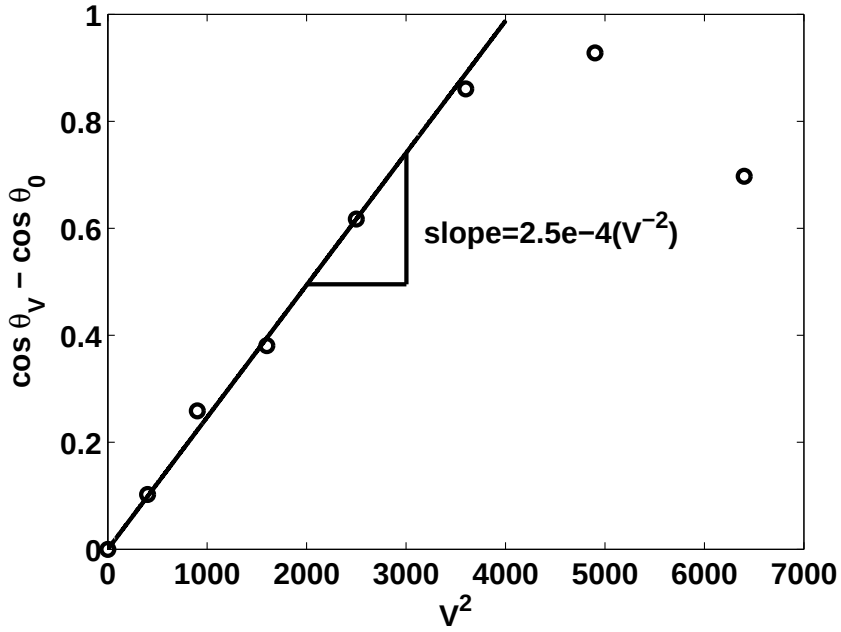

Figure 2.2: Variation of the cosine of static contact angle with the square of the applied voltage.

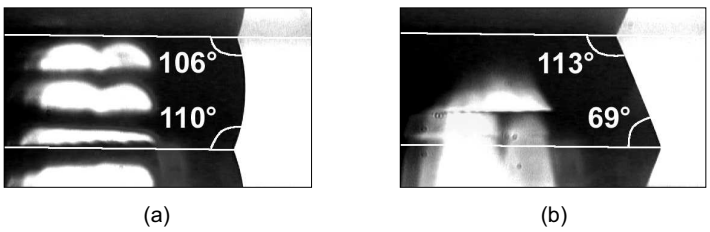

Figure 2.3: Static contact angles (±2°) of a deionized water drop between the two plates of a parallel-plate electrowetting device (a) before; (b) after the application of 50.2 V.

a deionized water drop in an electrowetting device with a top substrate both with and without an applied voltage. The increase of the top contact angle is of the same order of magnitude as the uncertainty in the measurement. Therefore, we ignore this small increase in our model and instead focus on the dramatic decrease of the contact contact angle, by about 40°, on the bottom substrate.

2.3 Dynamic measurements

2.3.1 Drop speed and morphologies

The average velocity of the glycerine-water drop in air is obtained by dividing the distance travelled by the time. Figure 2.4(a) shows that the drop remains static until a threshold voltage is reached. The threshold voltage to move a glycerine-water drop is approximately 38 V DC. The interface motion remains smooth for voltages up to 65 V DC as shown in figure 2.4(b). The average velocity of the drop, $\bar{u}$, increases linearly with the square of the applied voltage. The typical drop velocity ($\bar{u} \approx 0.1 - 1$ cm/s) indicates a small scaled Reynolds number, $Re^* = \alpha^2 \times \bar{u}R/\nu \sim O(10^{-2})$. At a higher voltage, we observed pinning on a section of the advancing (nose) contact line, causing the drop to form asymmetric shapes such as the one shown in figure 2.4(c). When moving a drop back and forth between two electrodes using such a high voltage, each drop movement becomes slower than the previous one. Eventually the drop stops responding to the applied voltage, suggesting an accumulation of charges trapped in the dielectric layers.

We now make a worst case estimate that the glycerine-water drop moving at $\bar{u} = 1$ cm/s has the same resistivity as a deionized water drop $r \sim 18.2 \times 10^4$ Ohm·m [LL87]. The ratio of charging time over the fluid convection time scale is $\bar{u}bcr/R \sim 6.6 \times 10^{-3}$. Therefore the formation of the electric double layer is much faster than the timescale of

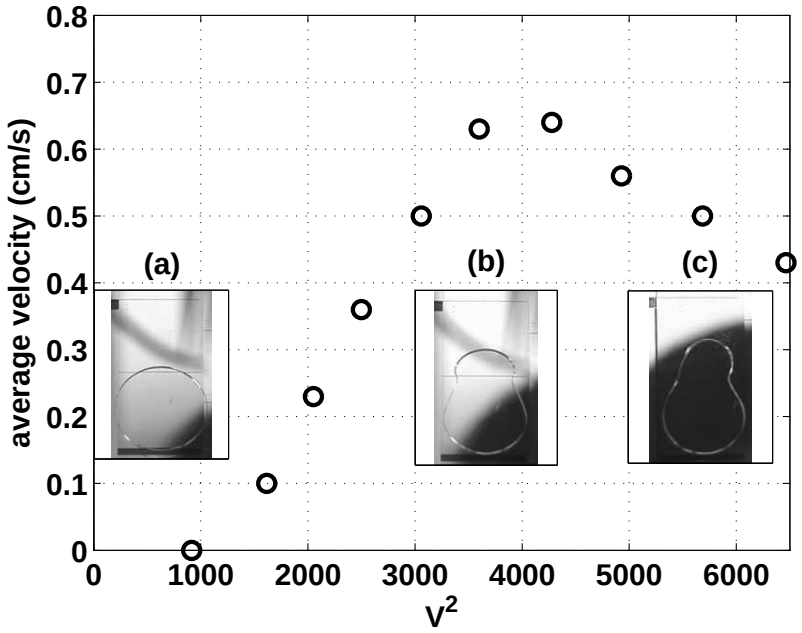

Figure 2.4: Average velocity of the drop actuated by electrowetting. Insets show (a) Static drop at low voltage (30.23 V DC); (b) Moving drop at 50.42 V DC. (c) Asymmetric drop shape due to pinning of the contact line at 80.0 V DC.

fluid convection, allowing us to equate the local surface energy change with a constant electrostatic energy stored across the dielectric film.

2.3.2 Dynamic contact angles

To fully understand the problem we must also measure the effect of electrowetting on the dynamic contact angles of the drop. The side views of the advancing meniscus is shown in figure 2.5. The location of the solid surfaces are depicted by two solid white lines. A dash line intersecting the substrates indicates the initial positions of the contact lines. The onset of electrowetting induces a sudden decrease of the contact angle on the bottom substrate from its static value $\approx 100^{\circ}$, as shown in figure 2.6. The capillary numbers of the contact lines, shown in figure 2.7, quickly settles down to

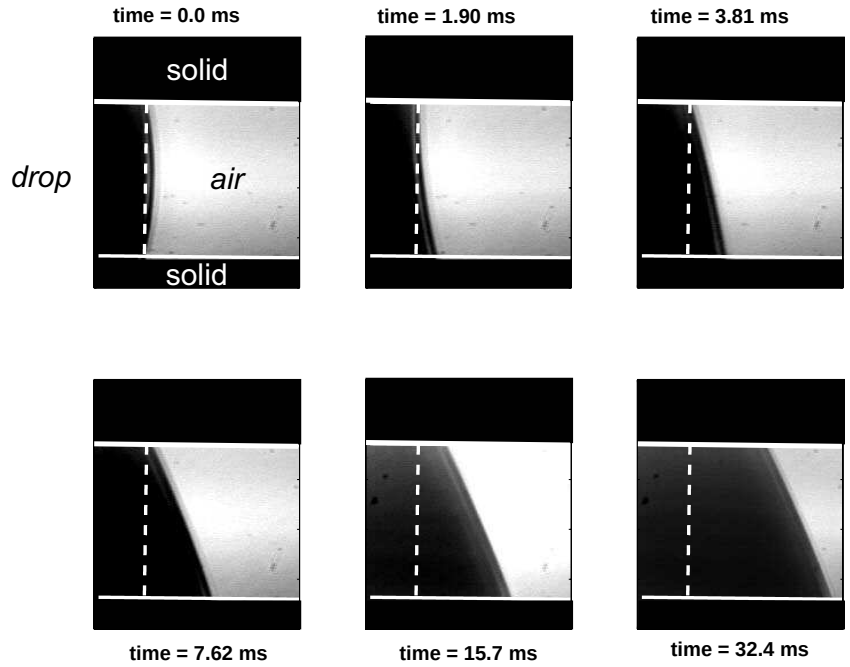

Figure 2.5: Side view of the advancing meniscus of a glycerine-water drop at 50.3 V DC. The dashed line shows the initial position of the meniscus.

the range of $Ca \sim 10^{-3}$. The contact line on the top substrate remains static until an angle of advance $\approx 110^{\circ}$ is exceeded. The hysteretic effect causes the initially concave meniscus to become convex. The contact angles converge toward steady state values after a short transient time. The steady behavior of the contact angle is consistent with the recent numerical finding of Yeo and Chang [YC06] for electrowetting films. The direct observation by the camera only reveals the contact angles at two points of the curvilinear interface. Along the interface, the capillary number varies with the normal velocity of the interface. Therefore, we expect the dynamic contact angles to vary along the interface. More advanced experimental techniques are required to characterize the evolution of the dynamic contact angle on the entire interface. In chapter 7 we will utilize the data to estimate the influence by the moving contact lines.

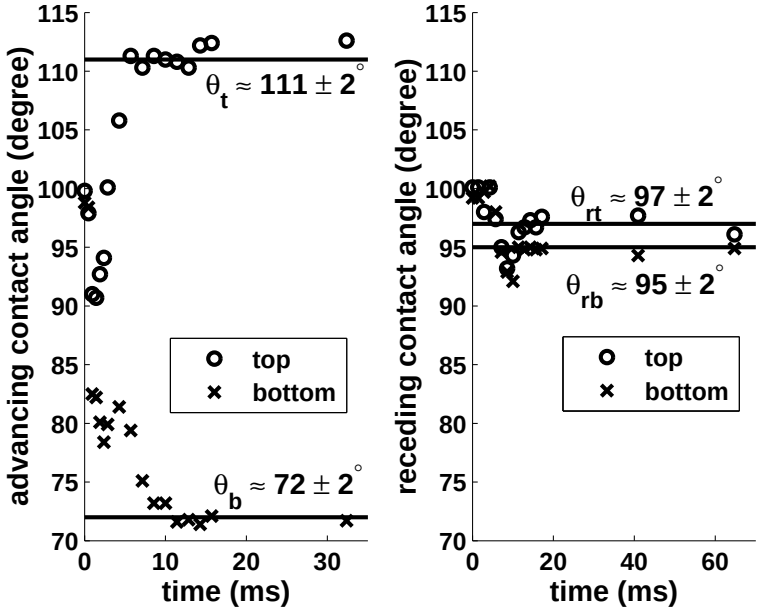

Figure 2.6: Evolution of the advancing and receding contact angles of the meniscus in figure 2.5.

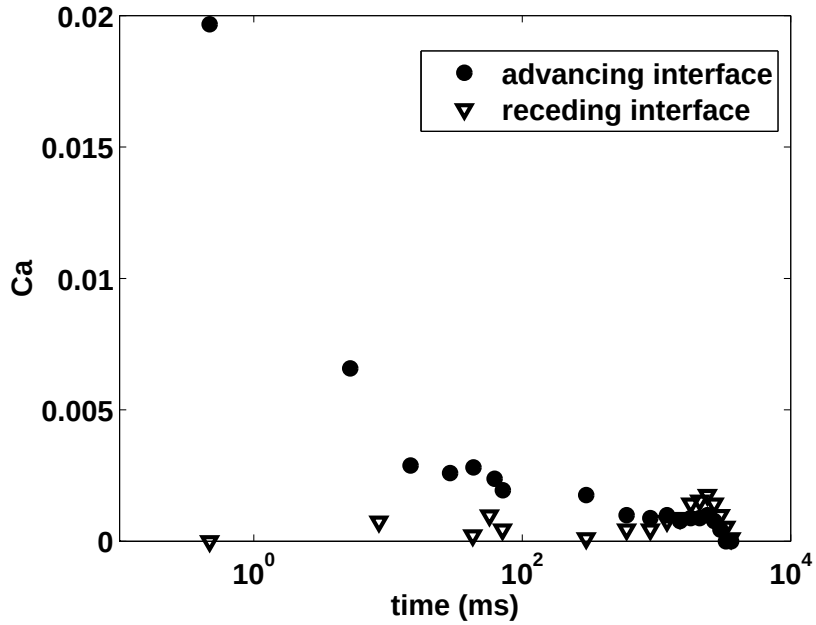

Figure 2.7: Capillary number of the advancing and receding meniscus.

CHAPTER 3

Sharp interface description

Here we derive the classical model of Hele-Shaw fluid dynamics and extend the model to include electrowetting. For simplicity, we will first neglect the presence of the contact line. The insight into the fluid dynamics will allow us to construct a simple leading order contact line model in chapter 7.

3.1 Lubrication theory

Consider a viscous drop occupying a space $[\Omega \times b]$, where b is the height of the Hele-Shaw cell. In absent of electrowetting, the drop relaxes to a circle of radius, R. In the case where $\alpha = b/R \ll 1$ is small, i.e. the drop is thin, we employ the lubrication theory to simplify the Navier Stokes equation. Let **V** denote a typical horizontal flow

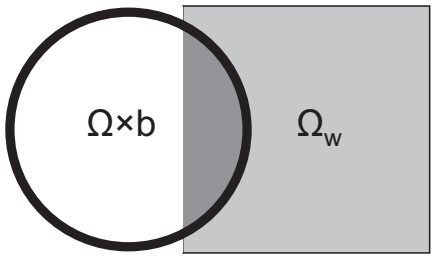

Figure 3.1: Top down view of a drop inside of a electrowetting device.

speed. The fluid observes no-slip boundary condition at $z = 0$ and $z = b$. This means the velocity $\mathbf{u}$ varies by $\mathbf{V}$ over a distance b. Therefore $\partial u/\partial z$ is of the order of $\mathbf{V}/b$ and $\partial^2 u/\partial z^2$ is of the order $\mathbf{V}/b^2$. In contrast the the variation of velocity in the horizontal direction scales as $\partial u/\partial x \sim \mathbf{V}/R$. The continuity equation,

$$\frac{\partial u}{\partial x} + \frac{\partial v}{\partial y} + \frac{\partial w}{\partial z} = 0, \tag{3.1}$$

then implies $w \sim \mathbf{V}b/R$. Apply the same scaling to the Navier stokes equation gives the following scalings

$$\begin{aligned} (\mathbf{u} \cdot \nabla)\,\mathbf{u} &\sim \frac{\mathbf{V}^2}{R}\left(1,\ 1,\ \frac{b}{R}\right), \\ \nu\frac{\partial^2 \mathbf{u}}{\partial z^2} &\sim \frac{\nu\mathbf{V}}{b^2}\left(1, 1, \frac{b}{R}\right), \end{aligned}$$

where ν is the kinematic viscosity. Comparison of the two terms shows the inertia is negligible if

$$\frac{\mathbf{V}R}{\nu}\left(\frac{b}{R}\right)^2 \ll 1. \tag{3.2}$$

Surprisingly, this condition is satisfied even if Reynolds number is not small. In addition to safely neglecting inertia, the viscous dissipation is dominated by shear across the depth of the Hele-Shaw cell. Therefore the Navier-Stokes equations reduces to

$$\begin{aligned} \frac{\partial p}{\partial x} &= \nu\frac{\partial^2 u}{\partial z^2}, \\ \frac{\partial p}{\partial y} &= \nu\frac{\partial^2 v}{\partial z^2}, \\ \frac{\partial p}{\partial z} &= \nu\frac{\partial^2 w}{\partial z^2}. \end{aligned}$$

Since w is smaller than the horizontal flow speed by a factor of b/R, the third equation shows the p is, to the first approximation, a function of only x and y. Integrating the first two equations with no-slip boundary condition at $z = 0$ and $z = h$ results Darcy's law coupled with a continuity equation,

$$\boldsymbol{U} = -\frac{b^2}{12\mu}\nabla P, \tag{3.3}$$

$$\nabla \cdot \boldsymbol{U} \;=\; 0, \tag{3.4}$$

where $\boldsymbol{U}$ is the depth-averaged velocity, P is the pressure in the drop or the bubble, and μ is the viscosity. Equations (3.3) and (3.4) imply the pressure is harmonic, $\triangle P = 0$.

The interfacial velocity is the fluid velocity normal to the interface, $\boldsymbol{U}_n \sim \nabla P|_{\partial\Omega} \cdot \hat{\boldsymbol{n}}$. The boundary condition for normal stress depends on the interactions between the different dominant forces in the meniscus region. Assuming pressure in the surrounding fluid is zero,

$$P|_{\partial\Omega} = \gamma_{lv} \left(A\kappa_0 + B\kappa_1 \right). \tag{3.5}$$

κ_0, defined as $1/r$, is the local horizontal curvature and κ_1 is defined as $2/b$. Different dynamics and wetting conditions at the meniscus determine the actual curvatures of the drop through A and B. In their initial study, Saffman and Taylor [ST59] made the assumptions that $A = 1$ and $B = -\cos\theta_A$ where θ_A is the apparent contact angle measured from inside of the drop or bubble.

For the incomplete displacement of viscous fluid, Bretherton [Bre61] showed that $B = 1 + \beta Ca^{2/3}$ where β is equal to 3.8 and -1.13 for advancing and receding menisci respectively. Higher order perturbation further showed that $A = \pi/4 + O\left(Ca^{2/3}\right)$ [PH84, Rei87]. For the special case of a complete displacement by a steady state finger as considered by Weinstein et al. [WDU90], the boundary condition can also be formulated in the form of equation (3.5). In this case, $B = -\cos(\Theta_R - \sigma\cos\Phi)$ where Θ_R is the angle of recede for the displaced fluid, $\sigma = \partial\Theta/\partial U$ is a linear model for the dynamic contact angle, and Φ is the angle between the outward normal of the steady state finger and the velocity U. For a partially wetting drop, we assume that $A = 1$, which is supported a posteriori in appendix B.

3.2 Electrowetting model

When a voltage is applied across an electrode, $V(x) = V\chi(x)$, where $\chi(x)$ is a characteristic function of the electrode, Ω_w, it locally decreases the solid-liquid surface energy inside the region $\Omega_w \bigcap \Omega$

$$\gamma_w(V) = \gamma_{lv}\left(-\cos\theta_0 - \frac{cV^2}{2\gamma_{lv}}\right), \tag{3.6}$$

where $\gamma_w(V)$ is the difference between the liquid-solid and the solid-vapor surface energy. In deriving (3.6), we assume the electrowetting does not affect the solid-vapor surface energy. From the experimental observation, only the dielectric layer on the bottom substrate produces significant electrowetting effect. Therefore, the solid-liquid surface energy of a drop in the device is

$$\gamma_{dev} = \gamma_{lv}\left(-2\cos\theta_0 - \frac{cV^2}{2\gamma_{lv}}\right). \tag{3.7}$$

The dominance of surface tension allows us to assume a circular profile for the liquid-vapor interface. Substituting (2.1) into (3.7) gives

$$\gamma_{dev} = \gamma_{lv}(-\cos\theta_0 - \cos\theta_V) = \gamma_{lv} b\kappa_w, \tag{3.8}$$

where $\kappa_w = (-\cos\theta_0 - \cos\theta_V)/b$ is the curvature of the cross substrate interface in the presence of electrowetting. The constant $\cos\theta_0$ does not affect the dynamics, so we will consider it to be zero. Equating $\kappa_w = B\kappa_1$ shows $B = -cV^2/4\gamma_{lv}$.

For a drop of volume v placed inside of a Hele-Shaw cell with plate spacing of b, the radius is $R = (v/\pi b)^{1/2}$. We non-dimensionalize the Hele-Shaw equations by the following scales:

$$r \sim R\tilde{r},\ t \sim \frac{12\mu R}{\gamma_{lv}\alpha^2}\tilde{t},\ P \sim \frac{\gamma_{lv}}{R}\tilde{P},\ (x, y, z) \sim (R, R, b). \tag{3.9}$$

Removing the ˜ gives the following equations in dimensionless variables:

$$\triangle P = 0, \tag{3.10}$$

$$\boldsymbol{U} = -\nabla P, \tag{3.11}$$

$$P|_{\partial\Omega} = A\kappa_0 + B\kappa_1, \tag{3.12}$$

$$\boldsymbol{U}_n = \nabla P|_{\partial\Omega} \cdot \hat{\boldsymbol{n}}. \tag{3.13}$$

In dimensionless terms, $\kappa_1 = 2/\alpha$ reflects the ratio between liquid-vapor and solid-liquid interfacial areas, and $B = -cV^2/4\gamma_{lv}$ reflects the ratio of the associated surface energies. $B\kappa_1$, dominates the pressure boundary condition of an electrowetting drop due to the small aspect ratio, α. Without the applied voltage, $V = B = 0$, the drop relaxes by surface tension. The constant A can then be incorporated into the relaxation timescale. Therefore, the classical relaxation of Hele-Shaw droplets has no dimensionless parameters, meaning all drops starting from similar initial conditions can be collapsed to the same problem in dimensionless form.

Electrowetting introduces a discontinuous change of the capillary pressure, $(P_2 - P_1) = -B\kappa_1$, as shown in figure 3.2. Solving the Laplacian pressure and the associated velocity near the discontinuity gives

$$P = -\frac{B\kappa_1}{\pi} \arctan\left(\frac{y}{x}\right) + P_1, \tag{3.14}$$

$$U = -\nabla P = \frac{B\kappa_1}{\pi} \frac{\left(-y\hat{\mathbf{i}} + x\hat{\mathbf{j}}\right)}{x^2 + y^2}. \tag{3.15}$$

where $\hat{\mathbf{i}}$ and $\hat{\mathbf{j}}$ are the unit axes of a locally orthogonally coordinate. Near $\partial\Omega_w$, electrowetting pumps the fluid into the wetting region. Therefore $B\kappa_1$ dictates the timescale of the motion. Away from $\partial\Omega_w$, where $B\kappa_1$ is relatively constant, the drop relaxes to minimize the liquid-vapor interface and $A\kappa_0$ influences this relaxation timescale. This interaction introduces one dimensionless parameter to the classical Hele-Shaw flow.

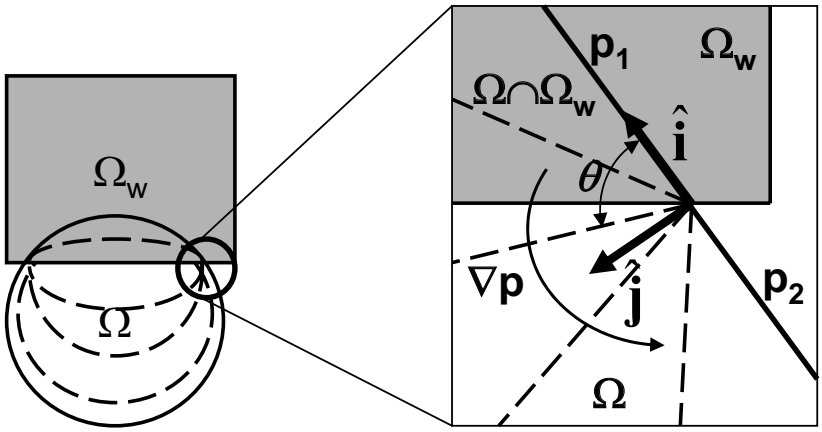

Figure 3.2: Illustration of electrowetting acting on a drop and the details near the boundary of electrode. Dashed lines depict the pressure contours.

We define the electrowetting number

$$\omega = -B\kappa_1 = \frac{cV^2}{2\alpha\gamma_{lv}}. \tag{3.16}$$

as the relative measure between the electrowetting potential and the total energy of the liquid-vapor interface. This parameter effects both the timescale of motion and the timescale associated with the drop morphology.

In applying the electrowetting model equation (3.16) for $B\kappa_1$, we assume the contact angles are determined from a quasi-static balance between the surface energies and the electrical potential. The presence of moving contact lines introduces deviations from the equilibrium values and reduces capillary pressure, $B\kappa_1$. In chapter 7, we will introduce the complication of contact line dynamics through the local dependence of A and B on the contact angles.

CHAPTER 4

Diffuse interface model

Diffuse interface (phase field) models have the advantage of automatically capturing topological changes such as drop splitting and merger. We extend Glasner's [Gla03] diffuse interface model to include electrowetting derived in the last chapter. Asymptotic expansions will then examine the relationship between the diffuse interface model and the sharp interface model.

4.1 Energy descriptions

The model begins with a description of the surface energies in terms of a "phase" function ρ that describes the depth-average of fluid density in a cell. Therefore $\rho = 1$ corresponds to fluid and $\rho = 0$ to vapor. Across the material interface, ρ varies smoothly over a length scale ϵ. The total energy is given by the functional

$$E(\rho) = \int_\Omega \frac{A}{\gamma}\left(\frac{\epsilon}{2}|\nabla\rho|^2 + \frac{g(\rho)}{\epsilon}\right) - \rho\omega \, dx. \tag{4.1}$$

The first two terms of the energy functional approximate the total liquid-vapor surface energy $\int_{\partial\Omega} \gamma dS$ where $\partial\Omega$ is the curve describing the limiting sharp interface. An interface of thickness ϵ is established through a competition between the interfacial energy associated with $|\nabla\rho|^2$ and the bulk free energy $g(\rho)$ that has two equal minima at ρ_l and ρ_v. Inspecting the two terms shows ϵ has the unit of length. Within this lengthscale, the phase variable varies smoothly from ρ_l to ρ_v. To avoid the degeneracy

in the resulting dynamic model (see equations 4.7-4.8) and to maintain consistency with the desired sharp-interface limit, we choose $\rho_l = 1$ and $\rho_v = \varepsilon$. The final term $\rho\omega$ accounts for the wall energy (the difference between the solid-liquid and solid-vapor surface energies) on the solid plates. The first two terms act as line energies around the boundary of the drop while the third term contributes the area energy of the solid-liquid interfaces. The sharp interface is represented by one of the closed contours of the phase field variable.

In equation (4.1), γ is a normalization parameter which we discuss below. A 1-D equilibrium density profile can be obtained by solving the Euler-Lagrange equation of the leading order energy functional in terms of a scaled spatial coordinate, $z = x/\epsilon$,

$$(\rho_0)_{zz} - g'(\rho_0) = 0, \tag{4.2}$$

which has some solution $\phi(z)$ independent of ϵ that approaches the two phases ρ_l, ρ_v as $z \to \pm\infty$. Integrating equation (4.2) once gives

$$\frac{\epsilon}{2}\phi_x^2 = \frac{g(\phi)}{\epsilon}. \tag{4.3}$$

Equation (4.3) implies equality between the first and second terms of the energy functional so the total liquid-vapor interfacial energy can be written as

$$\gamma = \int_{-\infty}^{\infty} (\phi)_z^2 dz = 2\int_{-\infty}^{\infty} g(\phi)\, dz. \tag{4.4}$$

Equation (4.4) indicates the choice of $g(\phi)$ used to model the bulk free energy influences the amount of interfacial energy in the model. Hence this constant appears as a normalization parameter in the first two terms of the energy functional (4.1).

Since there is no inertia in the physical system, the dynamics take the form of a generalized gradient flow of the total energy, which can be equivalently characterized as a balance between energy dissipation and the rate of free energy change,

$$D \approx \int_{R^2} \rho|\boldsymbol{U}|^2\, dxdy. \tag{4.5}$$

Since ρ is conserved, $\rho_t = -\nabla\cdot(\rho \boldsymbol{U})$. Using this fact and equating the rate of energy dissipation to the rate of energy change gives

$$\int_{R^2} \rho|\boldsymbol{U}|^2\, dxdy = -\int_{R^2} \rho_t \delta E\, dxdy = -\int_{R^2} \rho\nabla\left(\delta E\right)\cdot \boldsymbol{U}\, dxdy. \tag{4.6}$$

To make this true for an arbitrary velocity field $\boldsymbol{U}$, it follows that $\boldsymbol{U} = -\nabla\left(\delta E\right)$. Substituting the velocity back to the continuity gives the evolution of the fluid density,

$$\epsilon\rho_t = \nabla\cdot\left(\rho\nabla\left(\delta E\right)\right), \tag{4.7}$$

$$\delta E = \frac{A}{\gamma}\left(-\epsilon^2\triangle\rho + g'\left(\rho\right)\right) - \epsilon\omega, \tag{4.8}$$

subject to boundary conditions that requires no mass and surface energy fluxes at the domain boundary,

$$\nabla\rho\cdot\hat{\boldsymbol{n}} = 0, \tag{4.9}$$

$$\rho\nabla\left(\delta E\right)\cdot\hat{\boldsymbol{n}} = 0. \tag{4.10}$$

Equations (4.7-4.8) with $\omega = 0$ constitute a fourth order Cahn-Hilliard equation with a degenerate mobility term. By letting ω having spatial dependence, we introduce electrowetting into the diffuse interface model.

4.2 Asymptotic analysis

Matched asymptotic expansions show the sharp interface limit of the constant- mobility Cahn-Hilliard equation approximates the two-side Mullins-Sekerka problem [CF88, Peg89]. The recent work of Glasner [Gla03] showed the degenerate Cahn-Hilliard equation approaches the one sided Hele-Shaw problem in the sharp interface limit. Using a similar method, We show that the sharp interface limit of the modified Cahn-Hilliard equation (4.7-4.8) recovers the Hele-Shaw problem with electrowetting (3.10-3.13). The diffuse interface approximation allows us to enact topology changes without

artificial surgery of the contour. This is especially useful as electrowetting devices are designed for the purpose of splitting, merging and mixing of drops.

The diffuse interface model considers the bulk of the fluid as a region of a constant phase value, ρ_l and the air as a region of another constant phase value, ρ_v. The dynamics in these outer region are described by (4.7-4.8).

The interface is a thin, curved region of abrupt, but smooth transition from the fluid to the air over the length ϵ. Using a local orthogonal coordinate system (r, s), where s denotes the distance along $\partial\Omega$ and r denotes signed distance from the interface located at $r = Y(t)$. We define a scaled distance $z = (r - Y(t))/\epsilon$ for this inner region. The derivatives in (4.7-4.8) can be expressed in the new coordinate

$$\begin{aligned}
\rho_t &= \frac{\bar{\rho}_z}{\epsilon} r_t + \bar{\rho}_s s_t + \bar{\rho}_t \\
\nabla \cdot (\rho \nabla\ (\delta E)) &= \frac{\left(\bar{\rho}\left(\bar{\delta E}\right)_z\right)_z}{\epsilon^2} + \frac{\bar{\rho}\left(\bar{\delta E}\right)_z \triangle r}{\epsilon} + \bar{\rho}\left(\bar{\delta E}\right)_s \triangle s + \left(\bar{\rho}\left(\bar{\delta E}\right)_s\right)_s |\nabla s|^2 \\
\triangle \rho &= \frac{\rho_{zz}}{\epsilon^2} + \frac{\bar{\rho}_z \triangle r}{\epsilon} + \bar{\rho}_{ss} |\nabla s|^2 + \bar{\rho}_s \triangle s
\end{aligned}$$

where the $\bar{}$ denotes the variables in the inner region. The dynamic equation in the new coordinate is

$$\begin{aligned}
\epsilon^2 \bar{\rho}_z r_t + \epsilon^3 \left(\bar{\rho}_s s_t + \bar{\rho}_t\right) &= \left(\bar{\rho}\left(\bar{\delta E}\right)_z\right)_z + \epsilon \bar{\rho}\left(\bar{\delta E}\right)_z \triangle r + \\
&\quad \epsilon^2 \left[\bar{\rho}\left(\bar{\delta E}\right)_s \triangle s + \left(\bar{\rho}\left(\bar{\delta E}\right)_s\right)_s |\nabla s|^2\right], \qquad (4.11) \\
\bar{\delta E} &= \frac{A}{\gamma}\Big(- \bar{\rho}_{zz} - \epsilon \bar{\rho}_z \triangle r - \\
&\quad \epsilon^2 \left(\bar{\rho}_{ss} |\nabla s|^2 + \bar{\rho}_s \triangle s\right) + g'\left(\bar{\rho}\right)\Big) - \epsilon \omega \qquad (4.12)
\end{aligned}$$

We expand the variables in power series of ϵ

$$\begin{aligned}
\rho\left(x, t, \epsilon\right) &= \rho_0 + \epsilon \rho_1 + \epsilon^2 \rho_2 + \cdots, \\
\delta E\left(x, t, \epsilon\right) &= \delta E_0 + \epsilon \delta E_1 + \epsilon^2 \delta E_2 + \cdots,
\end{aligned}$$

and we similarly expands the variables in the inner region, $\bar{\rho}(r,t,\epsilon)$ and $\delta\bar{E}(r,t,\epsilon)$. After substituting these expansions into the equations (4.7-4.8) and (4.11-4.12), we solve the equations order by order of ϵ satisfying the boundary conditions at the domain boundaries. At an intermediate region, the solutions in the outer region and the inner region must match each other. The matching conditions are derived by formally equate the two expansions

$$\rho\left(x,t,\epsilon\right)=\bar{\rho}\left(Y\left(t\right)+\epsilon z,\epsilon\right), \tag{4.13}$$

and expand the right side by Taylor series in ϵ. There the expansion results

$$\bar{\rho}\left(z,\epsilon\right)=\sum_{n=0}^{N}\epsilon^{n}P_{n}\left(z,t\right)+\epsilon^{N+1}R_{N}. \tag{4.14}$$

P_n is the nth coefficient of the Taylor series

$$P_{n}=\frac{1}{n!}\frac{\partial^{n}}{\partial\epsilon^{n}}\bar{\rho}\left(Y\left(t\right)+\epsilon z,\epsilon\right)|_{\epsilon=0}. \tag{4.15}$$

Taking equation 4.13 to the limit of $z\rightarrow\pm\infty$ with $\epsilon z\rightarrow\pm 0$ gives

$$\bar{\rho}^{(0)}\left(z\right) \sim \rho^{(0)}\left(\pm 0\right),\ z\rightarrow\pm\infty,\ \epsilon z\rightarrow\pm 0, \tag{4.16}$$

$$\bar{\rho}^{(1)}\left(z\right) \sim \rho^{(1)}\left(\pm 0\right)+\rho_{r}^{(0)}\left(\pm 0\right)z,\ z\rightarrow\pm\infty,\ \epsilon z\rightarrow\pm 0, \tag{4.17}$$

$$\bar{\rho}^{(2)}\left(z\right) \sim \rho^{(2)}\left(\pm 0\right)+\rho_{r}^{(1)}\left(\pm 0\right)z+ \rho_{rr}^{(0)}\left(\pm 0\right)z^{2},\ z\rightarrow\pm\infty,\ \epsilon z\rightarrow\pm 0. \tag{4.18}$$

Similar conditions can be derived for $\delta\bar{E}$ and δE.

The $O\left(1\right)$ inner expansion gives

$$\left(\bar{\rho}^{(0)}\left(\delta\bar{E}^{(0)}\right)_{z}\right)_{z} = 0, \tag{4.19}$$

$$\frac{A}{\gamma}\left(g'\left(\bar{\rho}^{(0)}\right)-\bar{\rho}_{zz}^{(0)}\right) = \delta\bar{E}^{(0)}. \tag{4.20}$$

Equation (4.19) implies $\left(\delta E\right)^{(0)}=C\left(s,t\right)$. Equation (4.20) is the equation for the 1-D steady state. Integrating it once gives

$$\frac{\bar{\rho}_{z}^{(0)}}{2}=g\left(\bar{\rho}_{l}\right)-g\left(\bar{\rho}_{v}\right)+\delta\bar{E}\left(\rho_{l}-\rho_{v}\right). \tag{4.21}$$

For the solution to approach steady values as $z \to \pm\infty$, the right side must be zero. This can be satisfied uniquely by the common tangent construction,

$$\delta\bar{E}^{(0)} = \frac{\gamma\left(g\left(\rho_l\right) - g\left(\rho_v\right)\right)}{A\left(\rho_l - \rho_v\right)}. \tag{4.22}$$

The double well structure of $g\left(\bar{\rho}\right)$ implies $\left(\delta\bar{E}\right)^{(0)} = 0$. At the leading order, the competition between interfacial energy and the bulk free energy establishes a stable diffuse interface.

The $O\left(1\right)$ outer expansion of (4.7), (4.8) gives

$$\nabla \cdot \left(\rho^{(0)} \nabla g'\left(\rho^{(0)}\right)\right) = 0. \tag{4.23}$$

Making the substitution that $G\prime(\rho^{(0)}) = \rho^{(0)} g"(\rho^{(0)})$ gives

$$\triangle G(\rho^{(0)}) = 0 \tag{4.24}$$

with the no mass flux boundary condition and the matching boundary condition. The unique solution in the dense phase is a constant, $\rho^{(0)} = \rho_l$. Thus on an $O\left(1\right)$ scale no motion occurs.

The $O\left(\epsilon\right)$ inner expansion results

$$\left(\bar{\rho}^{(0)}\left(\delta\bar{E}^{(1)}\right)_z\right)_z = 0, \tag{4.25}$$

$$\frac{A}{\gamma}\left(g''\left(\bar{\rho}^{(0)}\right) - \frac{\partial^2}{\partial z^2}\right)\bar{\rho}^{(1)} = \delta\bar{E}^{(1)} - \frac{A}{\gamma}\kappa^{(0)}\bar{\rho}_z^{(0)} + \omega, \tag{4.26}$$

where the leading order curvature in the horizontal plane, $\kappa^{(0)}$, is identified with $-\triangle r$. Apply matching boundary condition for $\delta\bar{E}^{(1)}$ to equation (4.25) shows that $\delta\bar{E}^{(1)}$ is independent of z. $\bar{\rho}^{(1)} = \bar{\rho}_z^{(0)}$ is the homogenous solution of (4.26). In the region of constant ω, the solvability condition gives

$$\rho_l\left(\delta\bar{E}^{(1)}\right) = \frac{A\kappa^{(0)}}{\gamma}\int_{-\infty}^{\infty}\left(\bar{\rho}_z^{(0)}\right)^2 dz - \omega\rho_l. \tag{4.27}$$

The integral is equal to γ using (4.4). Assuming $\rho_l = 1$ and using (3.16) give

$$\delta\bar{E}^{(1)} = \left(A\kappa^{(0)} + B\kappa_1\right). \tag{4.28}$$

The surface energy term includes both curvatures of the interface. This is analogous to the Laplace-Young condition of a liquid-vapor interface.

In regions where sharp variation of ω intersects the diffuse interface, the solvability condition becomes

$$\rho_l\left(\delta\bar{E}^{(1)}\right) = A\kappa^{(0)} - \int_{-\infty}^{\infty} \omega\bar{\rho}_z^{(0)} dz. \tag{4.29}$$

The sharp surface energy variation is smoothly weighted by $\bar{\rho}_z^{(0)}$, which is $O(1)$ for a phase function $\bar{\rho}$ that varies smoothly between 0 and 1 in the scaled coordinate.

To order ϵ, the outer equation in the dense phase must solve

$$\triangle\left(\delta E^{(1)}\right) = 0, \tag{4.30}$$

with a no flux boundary condition in the far field, and a matching condition at the interface described by (4.17).

The $O\left(\epsilon^2\right)$ inner expansion reveals the front movement

$$U_n^{(0)}\bar{\rho}_z^{(0)} = \left(\bar{\rho}^{(0)}\left(\delta\bar{E}^{(2)}\right)_z\right)_z, \tag{4.31}$$

where r_t is identified as the leading order normal velocity of the interface $U_n^{(0)}$. Matching condition for $\delta\bar{E}^{(2)}$ can be simplified

$$\begin{aligned}
\delta\bar{E}^{(2)}(z) &\sim \delta E^{(2)}(\pm 0) + \delta E_r^{(1)}(\pm 0)\, z + \delta E_{rr}^{(0)}(\pm 0)\, z^2, \\
&\sim \delta E_r^{(1)}(\pm 0)\, z,\ z \to \pm\infty,\ \epsilon z \to \pm 0.
\end{aligned}$$

since $\delta E^{(2)}(\pm 0)$ is independent of z. This give us an equation for the normal interface velocity of drops in Hele-Shaw cell,

$$U^{(0)}|_n = -\left(\delta E^{(1)}\right)_r. \tag{4.32}$$

Defining $\tilde{p} = \delta E^{(1)}$, equations (4.28) (4.30) and (4.32) constitute the sharp interface Hele-Shaw flow with electrowetting,

$$\begin{aligned} \triangle \tilde{p} &= 0, \\ \tilde{p}|_{\partial\Omega} &= A\kappa^{(0)} + B\kappa_1, \\ U_n^{(0)} &= -(\tilde{p})_r \,. \end{aligned} \tag{4.33}$$

Therefore, the dynamics described by the diffused interface model approaches the sharp interface fluid dynamics in the Hele-Shaw cell as $\epsilon \to 0$.

CHAPTER 5

Biharmonic modified forward time-stepping

The nonlinear Cahn-Hilliard equation is one of a class of partial differential equations that arise in the study of thin films and phase field models. In general the equation is in the general form

$$u_t = \nabla \cdot (f(u) \nabla w), \tag{5.1}$$

$$w = -\triangle u + \phi', \tag{5.2}$$

where f is non-negative, and $u > 0$. Both f and ϕ' are smooth. We investigate the numerical properties of the biharmonic modified forward time-stepping for different variations of the forth order nonlinear equations (5.1-5.2). The finite difference in time is

$$\frac{u^{n+1} - u^n}{\Delta t} + M\Delta^2 u^{n+1} = \nabla \cdot ((M - f(u^n)) \nabla \Delta u^n) + \nabla \cdot \left(f(u^n) \nabla \phi'(u^n)\right). \tag{5.3}$$

We choose the scalar $M = k \max(f(u^n))$ and vary the value of k to investigate the effect of M on the numerical stability. The equation is discretized on a uniform cartesian mesh where $u^n_{i,j} = u(x_i, y_j, t^n)$, $x_i = i\Delta x$, and $y_j = j\Delta x$. We formulate the spatial finite difference in conservative form,

$$\mathbf{Q} = (p, q)^T = \left((M - f(u^n)) \nabla \Delta u^n + f(u^n) \nabla \phi'(u_n)\right), \tag{5.4}$$

$$\nabla \cdot \mathbf{Q} = \delta_x p + \delta_y q, \tag{5.5}$$

$$\delta_x p = \frac{\left(p_{i+1/2,j} - p_{i-1/2,j}\right)}{\Delta x}, \delta_y q = \frac{\left(q_{i,j+1/2} - q_{i,j-1/2}\right)}{\Delta x}.$$

The mobility terms at the midpoints of the mesh are approximated by trapezoidal averages

$$f\left(u_{i+1/2,j}\right) = f\left(\frac{1}{2}\left[u_{i,j} + u_{i+1,j}\right]\right), \tag{5.6}$$

and similarly for $f(u_{i,j+1/2})$. The spatial operators on u can then be formulated using second-order central difference on the existing grid points. We impose the Neumann boundary conditions on the domain boundary. The constant linear implicit operator can be inverted efficiently using fast Fourier transform. Similar ideas were also used to simulate coarsening in the Cahn-Hilliard equation [VR03] and surface diffusion [Sme03]. A step doubling scheme is used to adjust the simulation timesteps and a local extrapolation [PTV93] removes the $O(\Delta t)$ truncation error.

We first verify the convergence of the numerical scheme in the case of a well-known 2D self-similar solution of a simple forth order lubrication equation, which has a known self-similar solution. We will then illustrate interesting dynamics that arises in coarsening. The numerical results for the electrowetting microfluidics will be presented in the next chapter.

5.1 Lubrication equation

Defining $\phi' = 0$ and $f(u) = u$ reduces equations (5.1-5.2) to a nonlinear fourth order diffusion equation,

$$u_t + \nabla \cdot (u \nabla (\Delta u)) = 0. \tag{5.7}$$

The equation dissipates a free energy of the form

$$\frac{d\mathcal{E}}{dt} = -\int_\Omega |\nabla u|^2 dx \leq 0, \tag{5.8}$$

and models the diffusion of underground water in porous media. There exists a compactly-supported, d-dimensional, radially-symmetric self-similar solution [FB97]

$$u(\eta, t) = \begin{cases} \frac{1}{8(d+2)\tau^d}\left(L^2 - \eta^2\right)^2 & , \quad 0 \le \eta \le L \\ 0 & , \quad \eta > L, \end{cases} \tag{5.9}$$

$$\tau = \left[(d+4)(t+t_0)\right]^{1/(d+4)}, \tag{5.10}$$

where $\eta = r/t$. This solution is the higher order analogue of the Barenblatt-Pattle similar solution for the porous medium equation.

In additional to the stability constraint imposed by the forth order operator, the degenerate mobility requires a specialized numerical scheme to preserve positivity of the solution. We regularize equation (5.7) by replacing the degenerate mobility term with

$$f_\xi = \frac{u^5}{(\xi u + u^4)}. \tag{5.11}$$

$\xi = 10^{-10}$ so $f_\xi \sim u$ for $u \gg \xi$. Starting from a Gaussian, positive initial data

$$u(r, 0) = \varepsilon + \frac{\sigma}{40} e^{-\sigma r^2}, \tag{5.12}$$

where $r^2 = x^2 + y^2$. We expect a positive solution for all times, for small enough Δt [ZB00]. We solve equation (5.7) on a 50×500 mesh with $\Delta x = 0.02$. The parameter $\varepsilon = 0.01$ specifies a small thickness of the precursor film. Figure 5.1b shows the solution initially spreads isotropically with the $u(r, t) \sim t^{1/3}$ scaling law of the similarity solution. Due to the high aspect ratio of the computational domain, the diffusion across the shorter dimension saturates in $t \sim \mathrm{O}\left(10^{-3}\right)$, reducing the evolution afterward to an one dimensional problem where $u(y, t) \sim t^{-1/5}$.

In additional to the dissipation of the free energy, we can derive an estimate for the numerical scheme. Taking the inner product with $-\triangle u^{n+1}$ gives

$$\left(\nabla\left(u^{n+1} - u^n\right), \nabla u^{n+1}\right) + \Delta t M \|\nabla \Delta u^{n+1}\|_{L^2} = \Delta t \left(\nabla \Delta u^{n+1}, \left(M - f\left(u^n\right)\right) \nabla \Delta u^n\right). \tag{5.13}$$

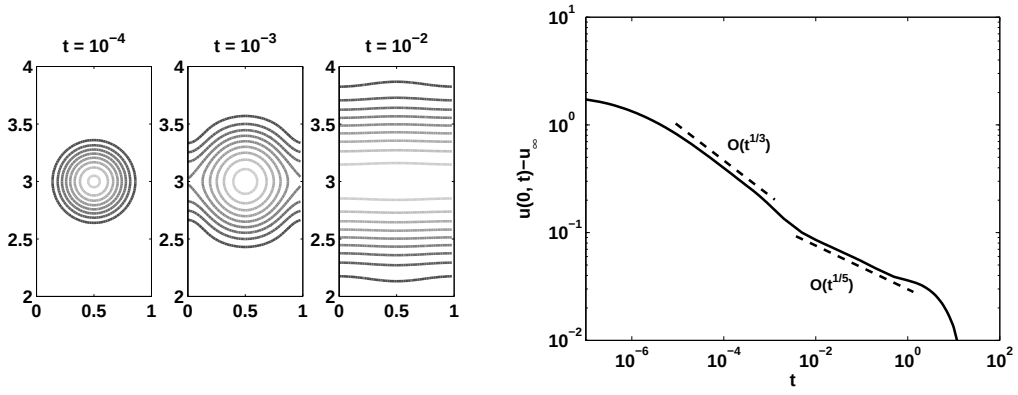

(a) (b)

Figure 5.1: (a) Contours of the simulated nonlinear diffusion with $k = 3.0$ and $\sigma = 80$. (b) Convergence of the simulation to the scaling laws of the similarity solution.

For $k \geq 1$, our choice of M is always greater than $\|f(u^n)\|_\infty$. We can bound the right side with

$$\Delta t \left(\nabla \Delta u^{n+1}, (M - f(u^n)) \nabla \Delta u^n \right) \leq \frac{\Delta t M}{2} \left(\|\nabla \Delta u^{n+1}\|_{L^2}^2 + \|\nabla \Delta u^n\|_{L^2}^2 \right), \tag{5.14}$$

since $f(u_n) \geq 0$. Some algebra will show the first term of equation (5.13) is

$$\left(\nabla \left(u^{n+1} - u^n \right), \nabla u^{n+1} \right) = \frac{1}{2} \|\nabla u^{n+1}\|_{L^2}^2 - \frac{1}{2} \|\nabla u^n\|_{L^2}^2 + \frac{1}{2} \|\nabla \left(u^{n+1} - u^n \right)\|_{L^2}^2. \tag{5.15}$$

Substituting into equation (5.13) gives us a bound of the quantity $F = \|\nabla u\|_{L^2}^2 + \Delta t M \|\nabla \Delta u\|_{L^2}^2$ at $u = u^{n+1}$ by the same quantity of the previous time step when $u = u^n$,

$$\|\nabla u^{n+1}\|_{L^2}^2 + \Delta t M \|\nabla \Delta u^{n+1}\|_{L^2}^2 \leq \|\nabla u^n\|_{L^2}^2 + \Delta t M \|\nabla \Delta u^n\|_{L^2}^2. \tag{5.16}$$

As shown in figure 5.2, the biharmonically modified algorithm dissipates F as required by equation (5.16). This provides an convenient way for debugging the algorithm.

At various stages of the evolution, we determine the maximum gradient stable timestep, Δt_g and the maximum positivity preserving timestep, Δt_p. As shown in figure

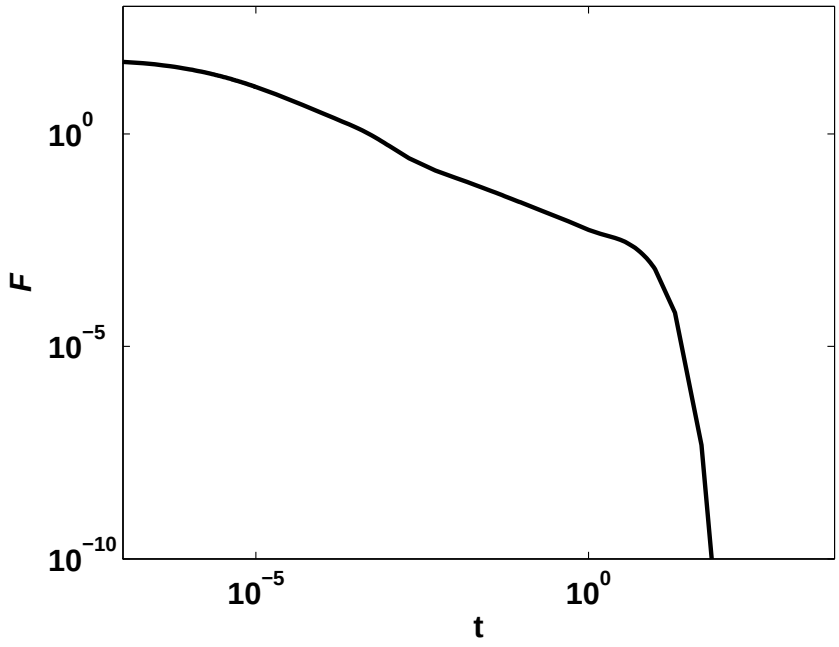

Figure 5.2: Monotonic decrease of the energy estimate, F. Simulation computed using $k = 3.0$.

5.3a, Δt_g increases with the value of k. As the solution smoothes sufficiently beyond $t \sim 10^{-2}$, unconditional gradient stability is achieved for $k \geq 1.0$. However, figure 5.3b shows the positivity preserving criterion imposes a stiffer stability requirement that is relatively independent of the value of k.

The accuracy requirement imposes another limiting factor in the simulation. In appendix A, we derived the modified equation for the the biharmonic modified scheme in one dimension

$$\begin{aligned} u_t + (\mathcal{F}(u))_x &= -\Delta t \left[\left(\frac{\partial \mathcal{F}}{\partial u} (\mathcal{F}(u))_x \right)_x - M (\mathcal{F}(u))_{xxxxx} \right] + O\left(\Delta x^2 + \Delta t^2\right), \\ \mathcal{F}(u) &= u u_{xxx}. \end{aligned} \tag{5.17}$$

The first $O(\Delta t)$ term is the truncation error of the forward Euler timestepping. The biharmonic modification contributes a non-local term in the truncation error. Starting

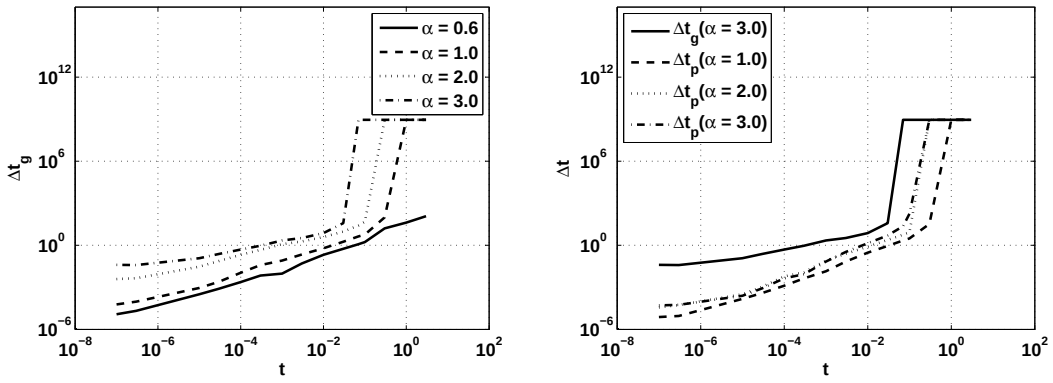

(a) (b)

Figure 5.3: (a)Maximum gradient stable timestep, Δt_g. (b)Maximum positivity preserving timesteps, Δt_p, computed with various values of k compared with Δt_g computed with $k = 3.0$.

from one dimensional ($r = x$) gaussian initial conditions equation (5.12), with various σ, we compute the differences of the 1D numerical solutions obtained by the the biharmonic modified timestepping, $u_b(x)$, and by the forward Euler timestepping, $u_E(x)$, after a very small timestep, $\Delta t = 10^{-10}$. Assuming the numerical solutions approximate the gaussian initial conditions, with the characteristic dimensions $x \sim \sigma^{-1/2}$, the truncation error of the biharmonic modification then scales as $\|u_E - u_b\| \sim (\mathcal{F}(u))_{xxxxx} \sim \sigma^6$, as confirmed in figure 5.4a. Therefore, the choice of k must balance the requirements of numerical efficiency and accuracy. It will be interesting to develop a rigorous theory that systematically determines the optimal value of k.

For control of truncation error, we consider a step doubling scheme, which estimates the truncation error by monitoring, $\Delta u = u^{(1)} - u^{(2)}$, where $u^{(1)}$ is the solution after one step of size Δt, and $u^{(2)}$ is the solution after two steps of size $\Delta t/2$. The step

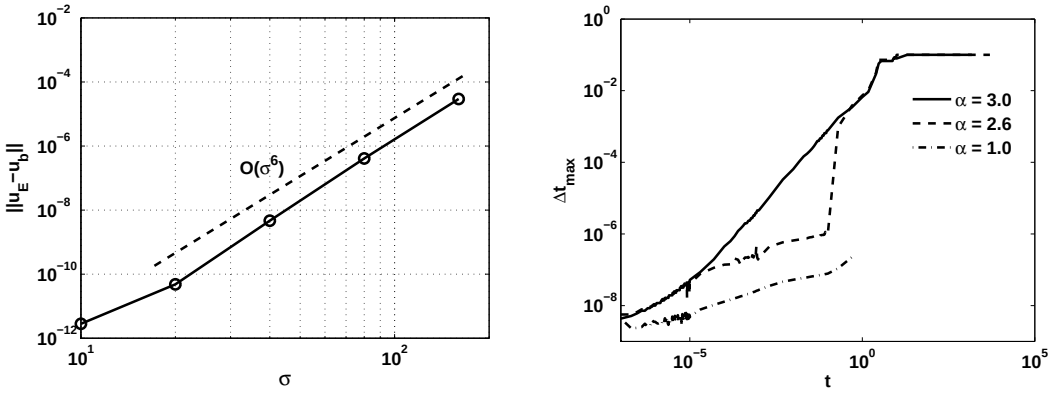

(a) (b)

Figure 5.4: (a)Scaling of the truncation error associated with the biharmonic modification. (b)Maximum timestep adopted by the step doubling scheme.

doubling adopts the timestep to satisfy a specific accuracy requirement:

$$\frac{2|\Delta u|}{u^{(1)} + u^{(2)}} < 10^{-5} \tag{5.18}$$

Figure 5.4b shows the maximum of the adaptive timesteps at various stages of the simulation shown in figure 5.1. The accuracy criterion places a more stringent constraint on the simulation than the gradient stability. The shape dependent truncation error of the biharmonic modification decreases with the gradient of the numerical solution, allowing the simulation to progressively increase the step size. In contrast, forward Euler timestepping is restricted by a constant stability constraint, $\Delta t \sim O(\Delta x^4) \cong 10^{-8}$. Increasing the value of k beyond 1 allows the simulation to take larger timesteps. Setting $k = 1$ constraints the $\Delta t \leq 10^{-6}$, making simulation to steady state impractical.

5.2 Degenerate Cahn-Hilliard equation

After studying the numerical behaviors of the biharmonic modified scheme, we now illustrate its application on the Cahn-Hilliard equation with degenerate mobility

$$\epsilon u_t = \nabla \cdot (u \nabla (w)), \tag{5.19}$$

$$w = \left(-\epsilon^2 \triangle u + \phi'(u)\right), \tag{5.20}$$

A double well function, $\phi(u) = (u-\varepsilon)^2(u-1)^2$, represents the bulk free energy of the material. The parameter ϵ determines the diffuse interface thickness by balancing the surface energy term, $|\nabla u|^2$, with the bulk free energy, ϕ.

Equations (5.19-5.20) were first introduced as a model for spinodal decomposition in binary alloys. Such coarsening phenomenon occurs in other systems such as multiphasic fluid and biological swarming. The growth of an ordered domain typically obeys the power law $L \sim t^n$ where L is the length scale of the domain [Bra94]. The detailed understanding of the scaling law, such as the value of n, is difficult to obtain analytically. Therefore, efficient simulation of the phase field model is important to the characterization of the coarsening process.

We initialize the phase field variable randomly on a mesh of size 240×240 with $\delta x = 0.03$. The diffuse interface thickness imposes a requirement on the grid resolution in order to resolve the transition layer, $\Delta x \leq C\epsilon$. The parameter $\epsilon = 0.0427$ controls the diffuse interface to be $\sim 7\Delta x$. Preconditioning techniques maybe implemented to relax this constraint [Gla01]. We did not employ preconditioning in this study.

Figure 5.6 shows the simulation of the coarsening process. The aggregation of the smaller drops produces irregular domain shapes with large curvatures, which drive the subsequent interface motion to relax the drop shapes toward circles. Equations

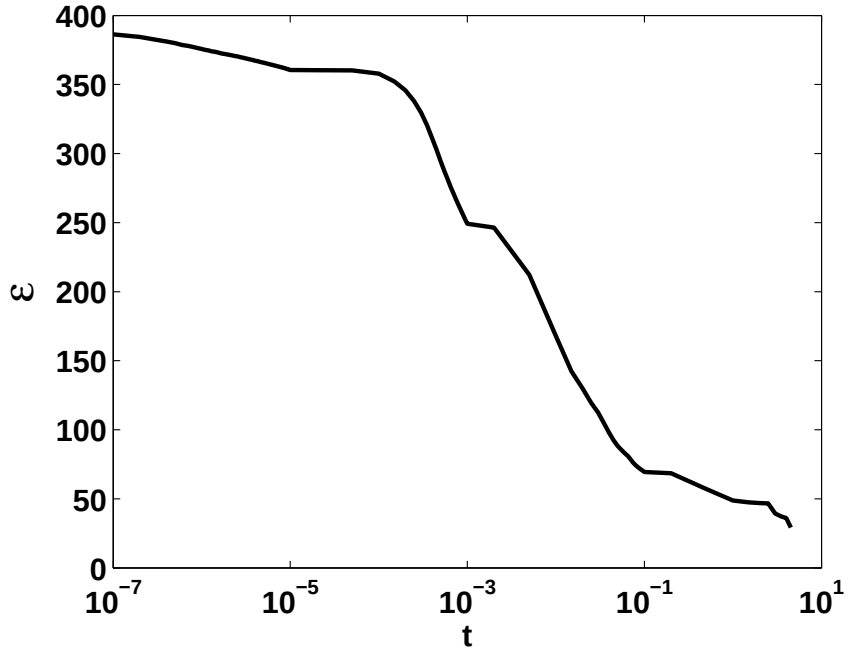

Figure 5.5: Monotonic decrease of the energy functional during the coarsening process.

(5.19-5.20) also have an energy functional of the form

$$\mathcal{E}(u) = \int_{\Omega} \frac{\epsilon^2}{2}|\nabla u|^2 + \phi(u)\, dx, \tag{5.21}$$

which must decrease monotonically for all solutions. Figure 5.5 shows that biharmonic modified timestepping reproduces such property of the problem.

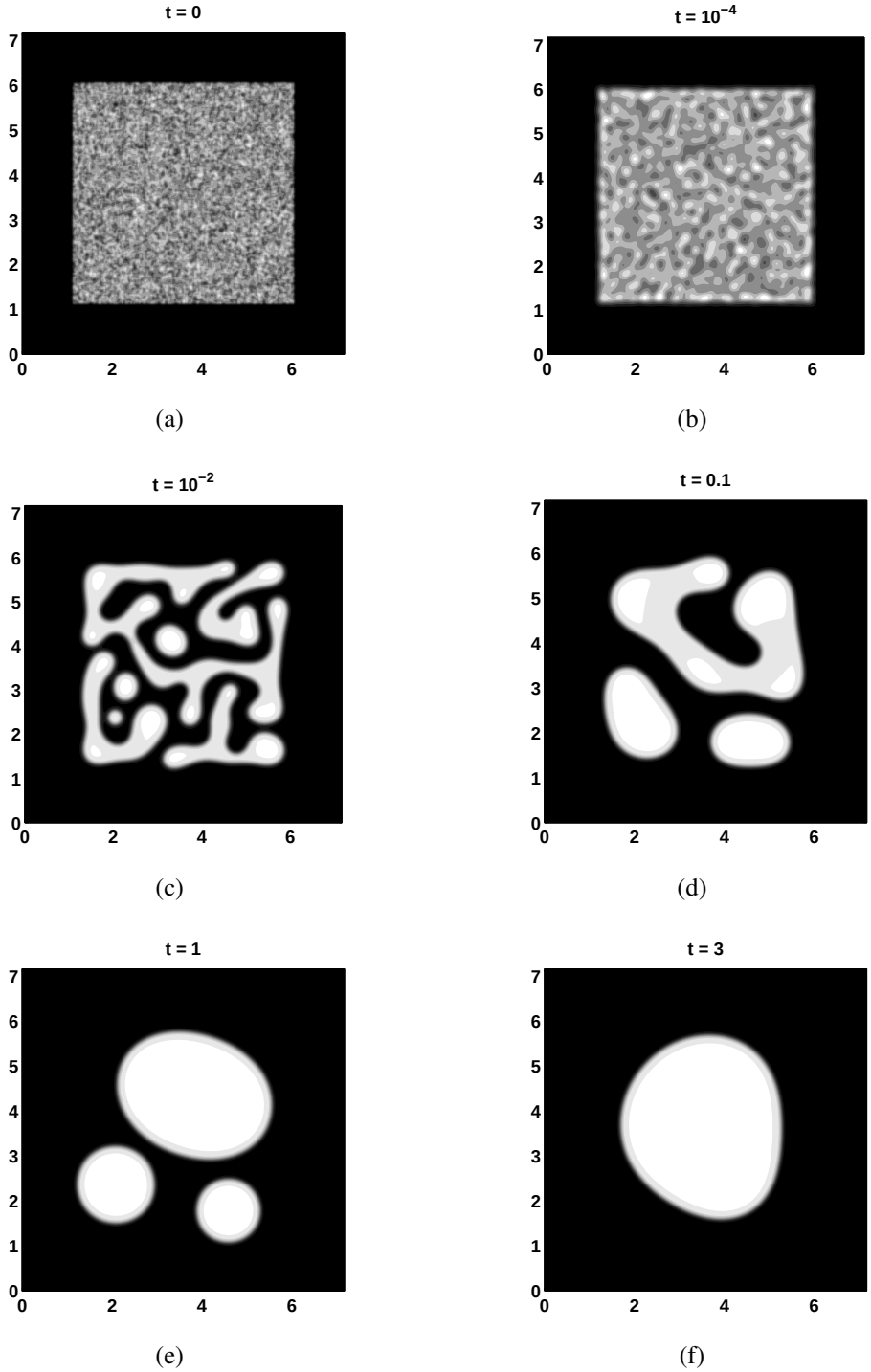

Figure 5.6: Simulation of coarsening from a uniformly distributed random initial condition.

CHAPTER 6

Numerical simulations and discussion

For a drop actuated by electrowetting in a Hele-Shaw cell, the non-linear Cahn-Hilliard equation is modified by a spatially dependent energy. We discretize the equations (4.7-4.8) using the biharmonic modified forward time-stepping

$$\epsilon\frac{\rho_{n+1}-\rho_n}{\Delta t}+\frac{A\epsilon^2 M}{\gamma}\Delta^2\rho_{n+1}=\frac{A}{\gamma}\left[\epsilon^2\nabla\cdot\left(\left(M-\rho_n\right)\nabla\Delta\rho_n\right)+\nabla\cdot\left(\rho_n\nabla g'\left(\rho_n\right)\right)\right]-\nabla\cdot\left(\rho_n\epsilon\omega\right). \tag{6.1}$$

We use a simple polynomial $g(\rho) = (\rho-\rho_v)^2(\rho-\rho_l)^2$. The choice of $g(\rho)$ imposes an artificial value of the liquid-vapor surface energy, γ. Integrating (4.4) gives the normalizing parameter, $\gamma = 0.2322$, for the terms associated with the liquid-vapor interface. All numerical results here are computed on a 256 by 128 mesh with $\Delta x = 1/30$. The origin is located at the midpoint of the electrode edge that intersects the drop interface as shown in figure 6.1. The parameter $\epsilon = 0.0427$ controls the diffuse interface thickness, which is $\sim 7\Delta x$ for all the results presented here.

The biharmonic modified scheme uses a scalar M that is large enough to improve the numerical stability. We found $M = \max(\rho)$ serves this purpose. To ensure the diffuse interface thickness of the simulation is in the range required by the asymptotic analysis, we performed simulations with smaller values of ϵ on refined meshes and verified that the timescale of motion is independent of $\epsilon \leq 0.0427$.

We compare the diffuse interface scheme against the boundary integral method by simulating the relaxation of an elliptical drop in a Hele-Shaw cell without electrowet-

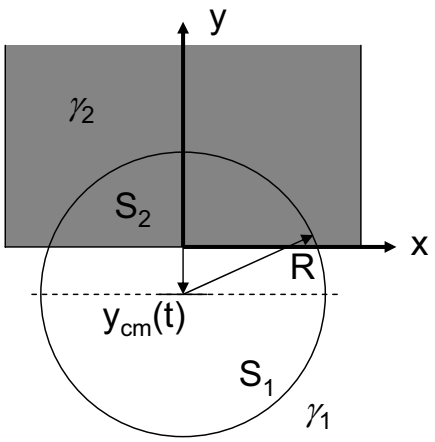

Figure 6.1: Coordinate of the numerical simulation.

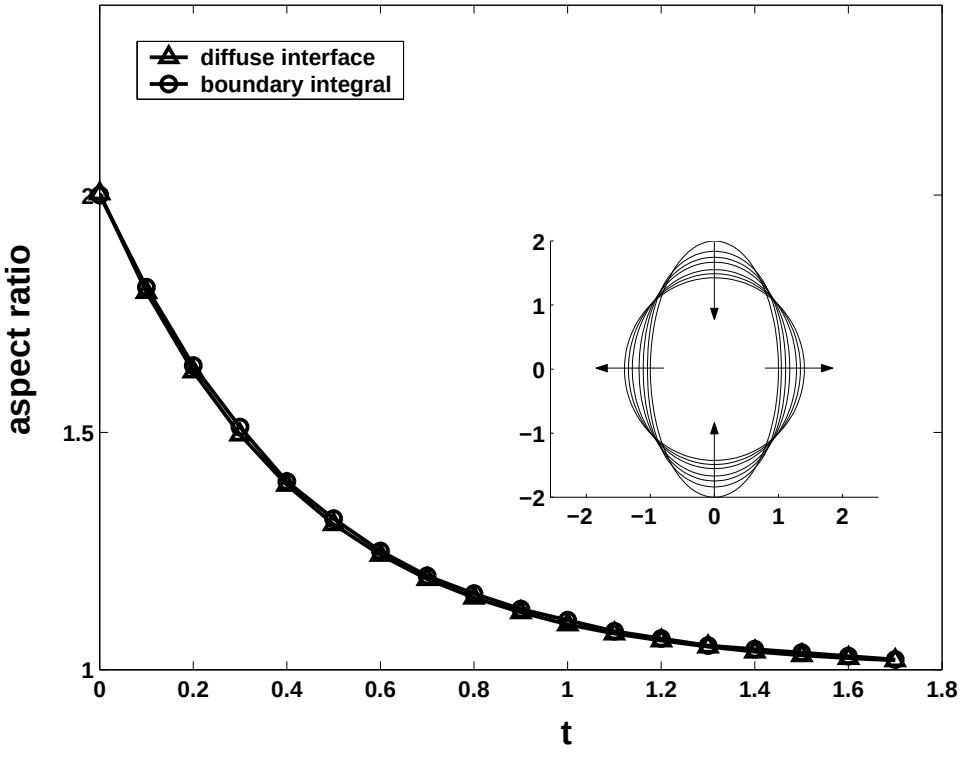

Figure 6.2: Aspect ratio of the relaxing elliptic drop calculated by diffuse interface model (△) with $\epsilon = 0.0427$ and boundary integral method, (○).

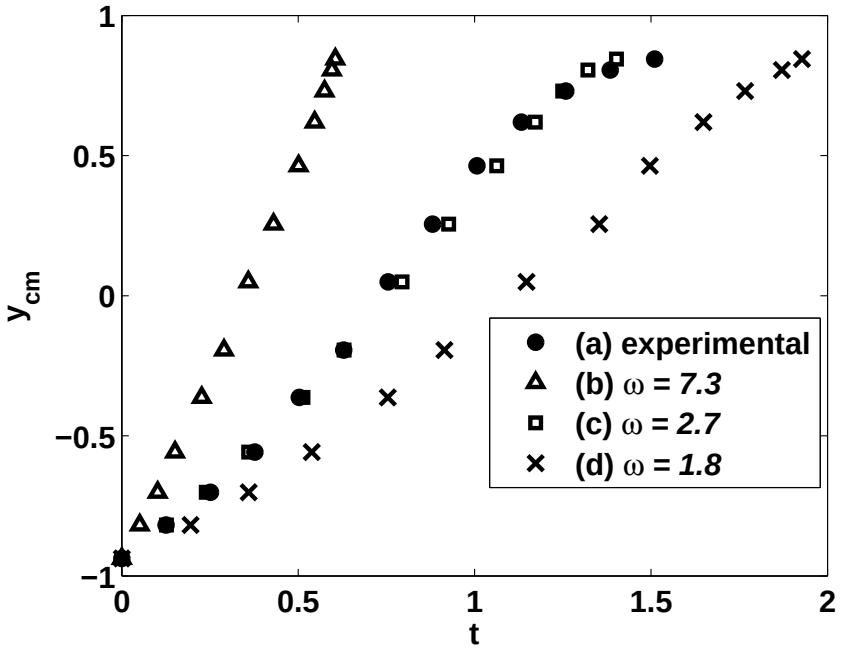

Figure 6.3: Positions of the center of mass of a moving drop in experiment and in simulations at various electrowetting number.

ting. Figure 6.2 shows a close agreement between the aspect ratios of the relaxing elliptic drops calculated by both methods.

To investigate the dynamics of an electrowetting drop without contact line dissipation, we directly compare the diffuse interface model with $A = 1$ to the electrowetting experiments using a glycerine-water drop. The experimental time and dimensions are scaled according to equation (3.9). The dimension of the square electrode is 10 mm. The initial radii of the drops in figures 6.5 and 6.6 are approximately 0.55 mm and 0.6 mm respectively. Using the capacitance per area, and the surface tension of the drop reported in §2, the experimental electrowetting numbers of $\omega_E = 7.3$ and 8.0 are derived for the drops under 50.4 V DC voltage.

Figure 6.3 compares the positions of an experimental drop's center of mass, $y_{cm}(t)$, against the simulation results at various ω. Figure 6.5 compares the corresponding

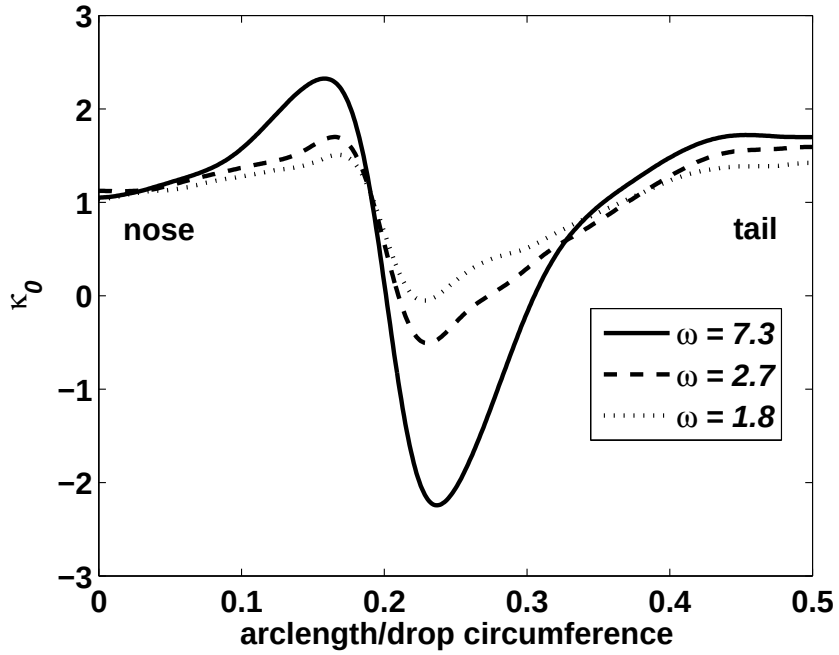

Figure 6.4: Curvature along the drop contours with $y_{cm} = -0.36$ from nose to tail.

drop contours. During the motion, electrowetting creates a necking region of negative curvature as shown in figure 6.4. As ω decreases, the variation of the curvature along the drop contour decreases due to the increasing influence of the surface tension. When $\omega = \omega_E$, the motion of the diffuse interface drop is faster than the experiment by a factor of 2. Scaling the electrowetting number to $\omega = 3/8\omega_E$ matches the simulation with the experimental motion and produces drop contours that qualitatively agree with the experiment as shown in figure 6.5(c).

Figure 6.6(a) shows the splitting of a drop. The asymmetry of the initial drop placement yields a difference in size of the daughter drops. Figure 6.6(b)-(d) illustrates the capability of the method to naturally simulate the macroscopic dynamics of a drop splitting. The simulation reproduces the dynamics of the bulk fluid through a gradient flow of the phase field variables such as shown in figure 6.7. As shown in figure 6.8, the dynamics monotonically dissipates the energy functional expressed in equation (4.1).

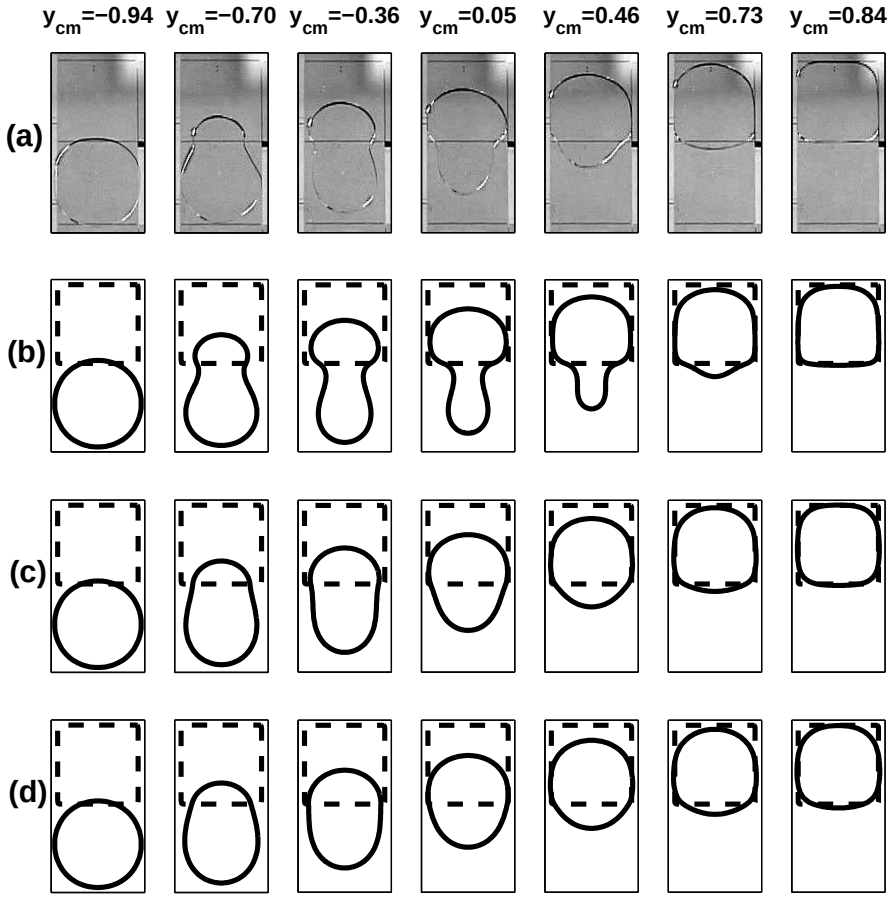

Figure 6.5: Drop movement by electrowetting: (*a*) experimental images of the drop under 50.4 volts of potential, (*b*) diffuse interface model with $\omega = 7.3$, (*c*) $\omega = 2.7$, and (*d*) $\omega = 1.8$. Each column shows the drop contours with the same center of mass position.

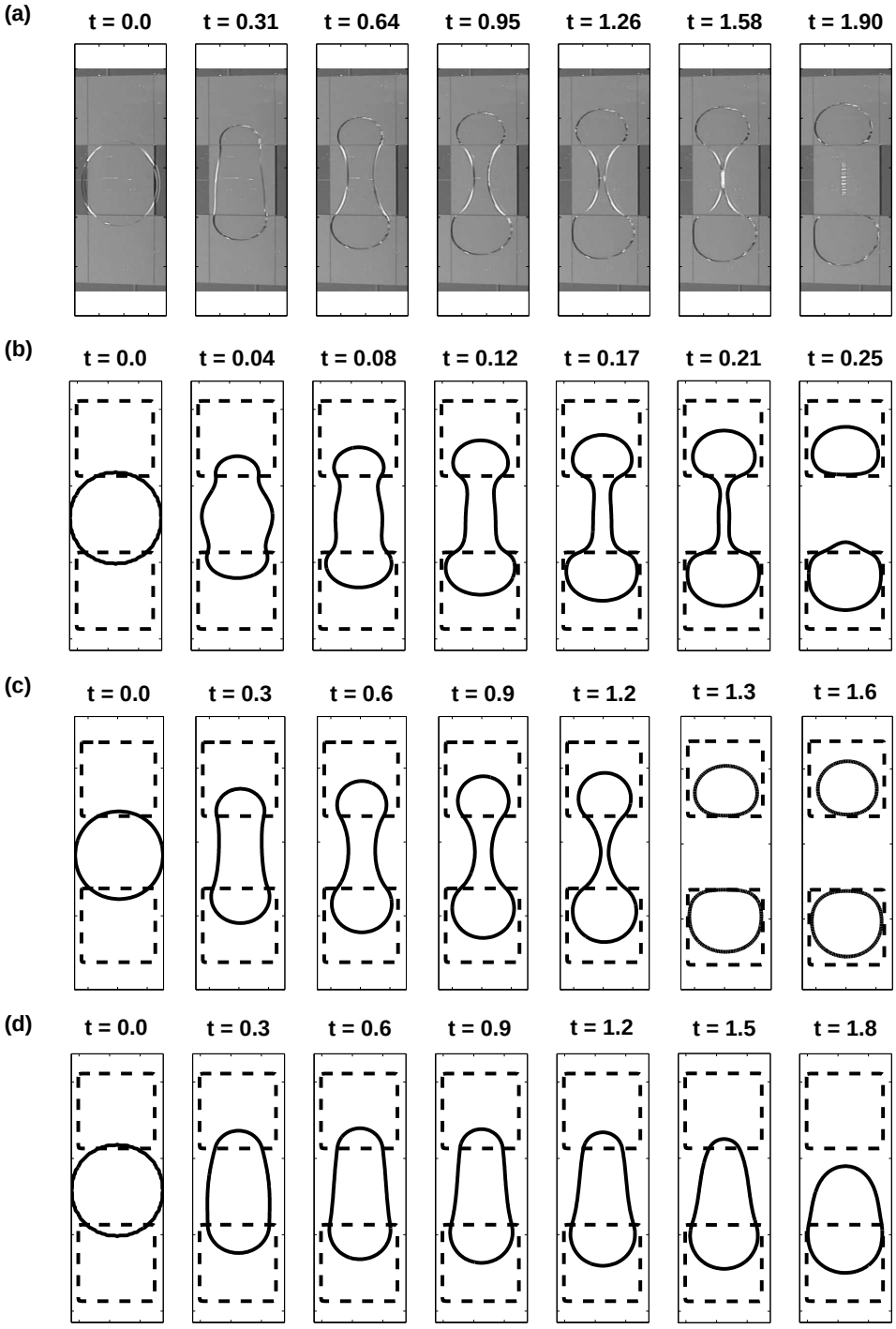

Figure 6.6: Drop splitting by electrowetting (*a*) images of a drop pulled apart by two electrodes under 50.4 volts of potential, (*b*) diffuse interface model with $\omega = 8.0$, (*c*) $\omega = 3.0$, and (*d*) $\omega = 2.0$.

The resolution of the model is limited by the diffuse interface thickness. Therefore we do not expect the simulation to reproduce the pinch-off of the neck and the formation of satellite drops, as seen in the last few frames of figure 6.6(a). Electrowetting initially stretches the drop, increasing the capillary pressure in the two ends and decreasing the pressure in the neck. For small ω, the electrowetting can not overcome the surface tension, which ultimately pumps the entire drop toward the end with smaller curvature as shown in figure 6.6(d). This is important for engineering application, since there is a geometric factor, b/R embedded in the definition of the electrowetting number. This indicates a challenge in splitting a thick drop by electrowetting, in agreement with Cho et al. [CMK03], who considers the capillary pressures at the neck and the two ends of the drop. When $\omega = \omega_E$, the timescale of drop splitting is faster in the simulation than in the experiment, by a factor of 8. In the next chapter, we show the contact line dynamics has a significant influence on the electrowetting number that is more than adequate to account for this discrepancy.

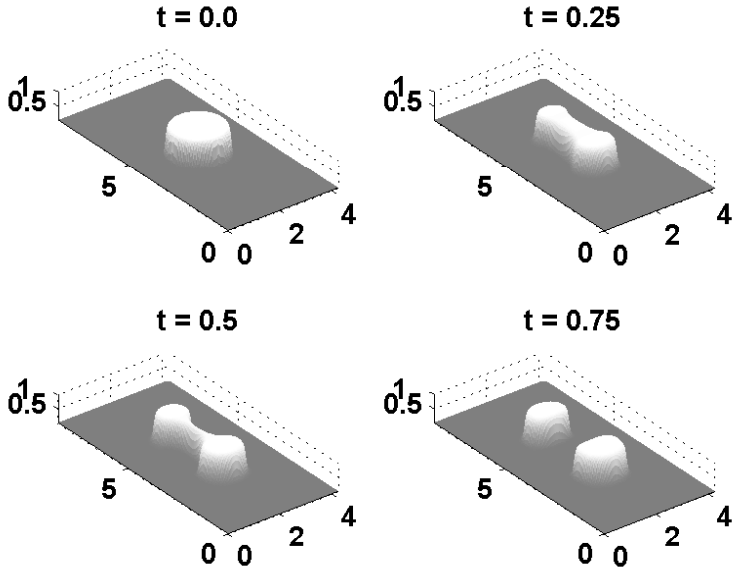

Figure 6.7: The 3 dimensional view of the phase field variables during the splitting of a Hele-Shaw drop by two local energies with $\omega = 3.6$.

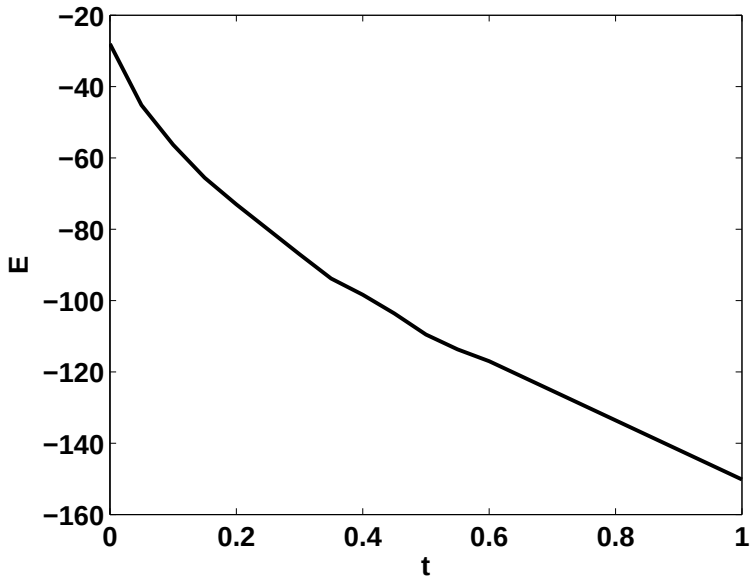

Figure 6.8: Monotonic decrease of the energy functional during the drop splitting with $\omega = 3.6$.

CHAPTER 7

Contact line effect

The previous sections investigated the drop dynamics in the absence of additional contact line effects due to the microscopic physics of the surface [deG85]. The diffused interface model has been used to study the dynamics near the contact line region of near-critical fluids [Sep96, Jac00].

Implementing a full contact line model for the Hele-Shaw drop requires knowledge of several microscopic parameters. For viscous fingering in a Hele-Shaw cell, Weinstein et al. [WDU90] incorporates a dynamic contact angle model into the capillary pressure. However, the asymptotic analysis of Weinstein et al. relies on a steady state assumption to avoid solving the leading order velocity in the inner region so the dynamic contact angle model only has geometric dependence on the finger shape. Thus their model is not directly applicable to our problem in which the interface dynamically changes in time. Therefore, how to consistently incorporate the dynamic contact angle into a general Hele-Shaw flow problem is still an interesting and open problem. Instead we estimate the influence of the contact line by a reduced order model with fixed contact angles. Similar contact line models have been used by Nadim and Ford [FN94] and Chen et al. [CTD05] in the context of thermally driven drops. Incorporating a fixed contact angle into the Hele-Shaw model requires a simple extension of the incomplete displacement problem and was first discussed by Saffman [Saf86]. We carry out the necessary asymptotic expansion in the limit of small aspect ratio and extend the formulation to an asymmetric electrowetting meniscus.

7.1 Reduced order model

The reduced order approximation considers a drop, in the sharp interface limit, travelling as a solid circle into a semi-infinite electrowetting retion. This allows us to isolate the timescale of the motion from the timescale associated with the shape morphology. Using the lubrication approximation, we balance the rate of viscous dissipation with the rate of free energy decrease,

$$D \approx -\frac{b^3}{12\mu}\int_{R^2}\rho|\nabla p|^2\,dxdy = -\frac{12\mu}{b}\int_{R^2}\rho|\boldsymbol{U}|^2\,dxdy = \frac{dE}{dt}. \tag{7.1}$$

The center of the circle travels along the axis as shown in figure 6.1. The distance between the boundary of electrowetting region and the origin is d. The position of the center is $y_0(t)$ where $y_0(0) = 0$. The drop moves as a solid circle so the integral reduces to

$$-\frac{12\mu|\dot{y}_{cm}|^2\pi R^2}{b} = \frac{dE}{dt}, \tag{7.2}$$

where $\dot{y}_{cm}$ denotes the velocity of the center of the circle. The free energy is composed of the surface energy of dielectric surface with no voltage applied γ_1, the surface energy of the electrowetting region γ_2, and the liquid-vapor surface energy. Since the liquid-vapor interface area remains constant, the rate of change in free energy is

$$\frac{dE}{dt} = \triangle\gamma\dot{S}_2, \tag{7.3}$$

where $\triangle\gamma = \gamma_2 - \gamma_1$ and $\dot{S}_2$ is the derivative of the drop area inside the electrified region with respect to time

$$\dot{S}_2 = -2R^2\sqrt{1-y_{cm}^2}\dot{y}_{cm}, \tag{7.4}$$

Equations (7.2), (7.3), and (7.4) give the following ODE:

$$\dot{y}_{cm} = \frac{b\triangle\gamma}{6\mu\pi R^2}\sqrt{1-y_{cm}^2}. \tag{7.5}$$

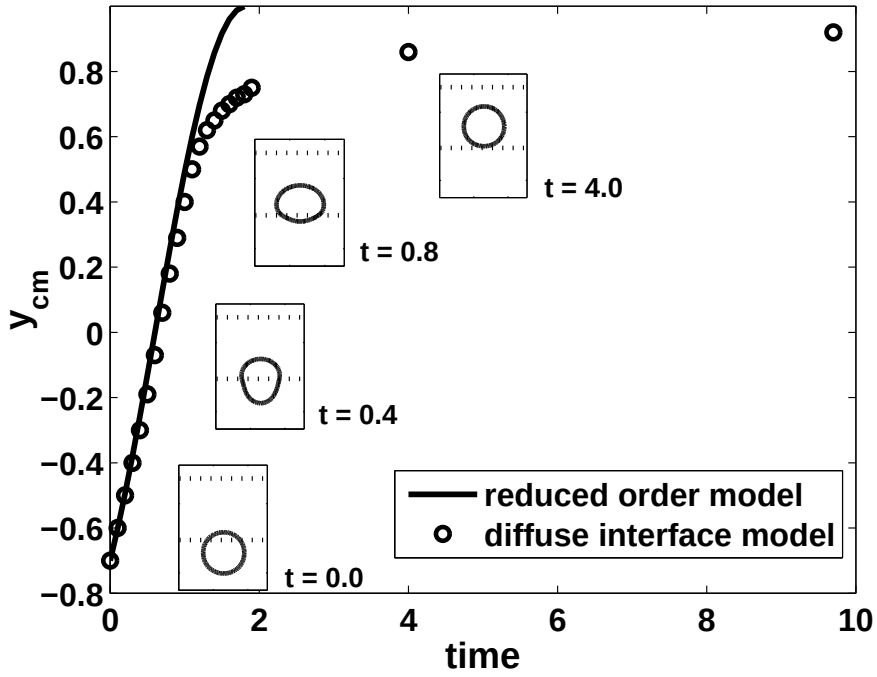

Figure 7.1: The centers of mass of the reduced order model and the diffuse interface model. $\epsilon = 0.0427$, $\omega = 5.0$.

Integrating this ODE, we get

$$y_{cm}(t) = \sin\left(\frac{b\triangle\gamma}{6\mu\pi R^2}t + C\right),\ C = \arcsin\frac{y_{cm}(0)}{R}, \tag{7.6}$$

If we neglect the surface effects, the energy difference between the two regions is well described by (1.1), $\Delta\gamma = -cV^2/2$. After changing time to a dimensionless variable, we get

$$y_{cm}(t) = \sin\left(\frac{-2\omega}{\pi}t + C\right),\ C = \arcsin\frac{y_{cm}(0)}{R}. \tag{7.7}$$

Figure 7.1 compares the center of mass of the reduced order model against the one in diffuse interface model. The ability of the diffuse interface drop to freely deform allows it to translate slightly faster into the electrowetting region. Once the entire drop mass has moved into the wetting region, a slow relaxation toward a circular shape takes

place. The close agreement in the translation period shows the diffuse interface model does accurately simulate the gradient flow of the energy functional. The discrepancies of timescale shown in figures 6.5 and 6.6 must be attributed to additional effects in the physical problem.

7.2 Deviation of pressure boundary condition

The deviations of contact angles from their equilibrium values changes the capillary pressure at the interface. The contact angles increase along the advancing contact lines and decrease along the receding contact lines. Here we relate the pressure boundary condition (3.5) to the local contact angle by perturbation expansions of the governing equations with respect to the aspect ratio by considering a radially expanding partially wetting fluid [Saf86]. We calculate the conditions for both the symmetric interfaces and the asymmetric interfaces as shown in figure 7.2. The interface moving with velocity U can be described by a function $z = h(r)$. The governing equations are the Stokes equations and the continuity equation.

$$\begin{aligned} u_r &+ \frac{u}{r} + w_z = 0, \\ p_r &= \mu\left(\Delta u - \frac{u}{r^2}\right), \\ p_z &= \mu\left(\Delta w\right). \end{aligned}$$

We introduces the dimensionless variables.

$$\begin{aligned} \tilde{r} &= \frac{r-R}{b},\ \tilde{z} = \frac{z}{b}, \tilde{h} = \frac{h}{b}, \\ \tilde{p} &= \frac{b}{\gamma_{lv}} p,\ \tilde{u} = \frac{u-U}{U},\ \tilde{w} = \frac{w}{U}. \end{aligned}$$

Following the common procedure of purterbation expansion, we expand the variables in terms of the small parameter $\alpha = b/R$. Up to $O(1)$, the only relevant equations

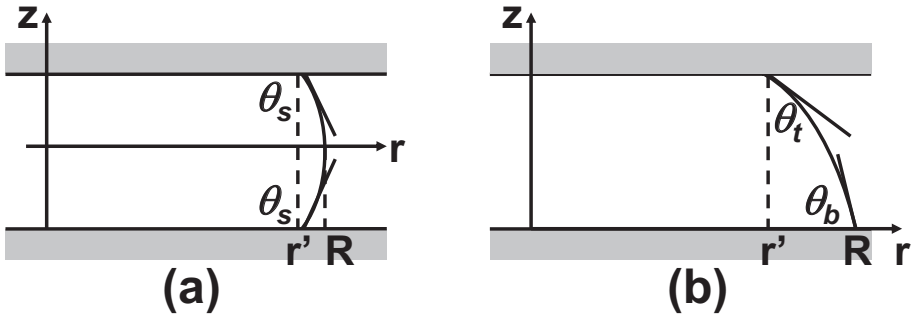

Figure 7.2: Coordinate and geometry of (a) a symmetric interface and (b) an asymmetric interface due to electrowetting.

to solve are the normal stress balances of the interface. The leading order equation in $O(\alpha^{-1})$ relates the cross substrate curvature, $B\kappa_1$, to the local contact angle, and the next order expansion corresponds to the contribution from the horizontal curvature, $A\kappa_0$.

Outside of the electrowetting region, the interface is symmetric as shown in figure 7.2a. The normal stress balance is

$$P^0|_{\partial\Omega} = -\frac{h^0_{rr}}{\left(1 + (h^0_x)^2\right)^{\frac{3}{2}}} \tag{7.8}$$

The equation is integrated twice with boundary conditions $h^0_r(R) = -\infty$ and $h^0(R) = 0$ to obtain $h^0(r)$. Applying the boundary conditions that $h^0(r') = 1$, where $r' = (1 - \sin\theta_s) / \cos\theta_s + R$ gives the leading order pressure.

$$P^0|_{\partial\Omega} = \frac{-2\cos\theta_s}{\alpha} \tag{7.9}$$

If the interface inside the electrowetting region satisfies the requirements that $\theta_t \geq \pi/2$ and $\theta_b \leq \pi/2$, as shown in figure 7.2b, similar expansions for the interface with a shifted coordinate gives the same equation (7.8) for the normal stress balance. Integrating it with the boundary conditions $h^0_r(R) = -\tan\theta_b$, $h^0(R) = 0$ and $h^0(r') = 1$,

where $r' = -(\sin\theta_t - \sin\theta_s) / (\cos\theta_t + \cos\theta_b) + R$.

$$P^0|_{\partial\Omega} = \frac{-(\cos\theta_b + \cos\theta_t)}{\alpha} \tag{7.10}$$

The capillary pressure difference across the electrowetting and the non-electrowetting regions in the leading order becomes

$$B\kappa_1 = \frac{(\cos\theta_r - \cos\theta_t + \cos\theta_r - \cos\theta_b)}{\alpha}. \tag{7.11}$$

where θ_r is the receding contact angle on the receding contact lines. θ_t and θ_b are the advancing contact angles on the top and the bottom substrates.

In absence of such deviations, the contact angles assume their equilibrium values, and the difference of capillary pressure is represented by the electrowetting number. Using (3.16) and (2.1) gives

$$\omega = -\frac{cV^2}{2\alpha\gamma_{lv}} = \frac{1}{\alpha}(\cos\theta_0 - \cos\theta_V). \tag{7.12}$$

Comparing equations (7.11) and (7.12) gives a scaling factor

$$\xi = \frac{B\kappa_1}{\omega} = \frac{(\cos\theta_s - \cos\theta_t) + (\cos\theta_s - \cos\theta_b)}{\cos\theta_0 - \cos\theta_V}. \tag{7.13}$$

where $\cos\theta_b < \cos\theta_V$, $\cos\theta_t < \cos\theta_0$, and $\cos\theta_r > \cos\theta_0$. It can be shown that the scalar ξ is less than 1. The change of the capillary pressure may be incorporated into the reduced order model by scaling the electrowetting number accordingly,

$$y_{cm}(t) = \sin\left(\frac{-2\xi\omega}{\pi}t + C\right). \tag{7.14}$$

Substituting in the measured values of contact angles from figure 2.6 gives an estimate of $\xi = 0.23$. This indicates the deviation of contact angle may reduce up to 3/4 of the capillary pressure difference and account for a four fold increase in the dynamic timescale.

The analysis in chapter 3 shows the velocity of the electrowetting drop is proportional to the difference of $B\kappa_1$ across the boundary of the electrowetting region. However, our estimate by the reduced order model imposes the measured contact angles at the nose and the tail over the entire electrowetting and non-electrowetting interfaces. Therefore we expect the reduction to $1/4$ of the experimental electrowetting number to yield an upper bound of the timescale increase due to the contact line effect. Figure 6.5(c)-(d) shows reducing ω accordingly in simulation indeed gives a range of timescale that includes the experimental timescale. The fitting factor for ω to match the simulated motion with the the experiment is $\xi = 3/8$, well within the bound of our estimate. The failure to split the drop as shown in figure 6.6(d) further confirms that the reduction overestimates the contact line effect. The simulation results in figures 6.5(c) and 6.6(c) indicate that further refinements with a dynamic contact angle model may substantially improve the agreement with the experiment.

In addition to its influence on the dynamic timescale, the contact angles also affect the morphology of the drop motion. Therefore, a complete model of the contact line dynamics needs to address both the effect on $A\kappa_0$ and $B\kappa_1$. This differs from the scaling factor in Walker and Shapiro [WS06] that phenomenologically modifies the dynamic timescale to fit with the experiments.

CHAPTER 8

Three-dimensional drops

In practice, the operating condition in an electrowetting device often violates the geometric assumption of a Hele-Shaw cell. As the drop evaporates, cuts, or merges, its radius changes to a length comparable to the separation height of a parallel plate electrowetting device. As the three dimensional (3D) drop moves across an electrode, its shape remains convex due to the dominance of surface tension. Fluid dynamics in the direction normal to the substrate becomes significant. In addition, the flow in such drop is more efficient than that in a Hele-Shaw drop for mixing application. Mixing in microscale remains a challenging task for continuous microfluidic technology, due to the laminar flow nature. In order to achieve folding and stretching of fluid material, the flow must be rotational. Many studies have proposed active [LST07, BCM07, RBH00] and passive methods [LSS00, SDA02, STI03] to generate mixing. Although droplet-based microfluidics is not continuous (e.g., a train of discrete droplets merging) and thus not expected to hold the same degree of difficulty in mixing that continuous microfluidics suffers from, the flow field within the droplets needs to be understood to evaluate the mixing. Within single sessile drops on single-plate EWOD devices, Aizenberg et al. [AKK06] and Mugele et al. [MBS06] demonstrated mixing by oscillation of the air-liquid interface. For a thin-flat drop in a parallel-plate electrowetting device, the fluid dynamics in the plane parallel to the substrate is irrotational. We can

show this by eliminating the pressure gradient in Darcy's Law (3.3). Doing so gives

$$\frac{\partial v}{\partial x} - \frac{\partial u}{\partial y} = 0, \tag{8.1}$$

where the left hand side is the definition of vorticity. Equation 8.1 shows the vorticity is zero everywhere on a horizontal plane. The only mixing is done by stretching and folding by the parabolic flow profile and the fluid recirculation at the drop interface. Figure 8.1 illustrates this behavior. Through a series of coalescence between clear and dyed (Mordant Blue 9) glycerin drops, a straight front of dyed fluid is formed inside the drop. As the drop moves to another electrode by electrowetting, the straight front remains relatively straight, trailed by the smearing produced by the parabolic flow profile. This flow behavior is due to the dominance of the viscous stress across the two

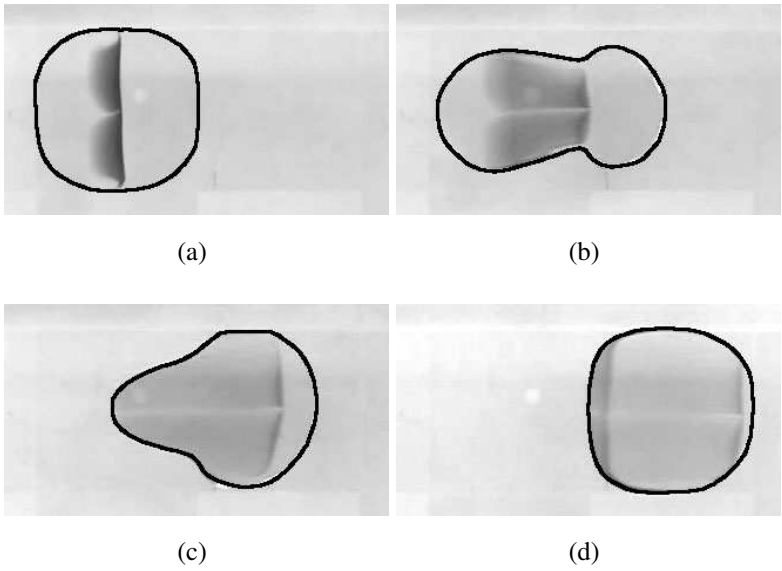

Figure 8.1: Mixing of dye in a Hele-Shaw drop actuated by electrowetting.

substrates. Therefore it is necessary to understand the fluid dynamics in a thick, 3D, drop in order to design sophisticated electrowetting devices for mixing. Such a drop constrained by two solid substrates couples the no-slip solid boundary with the free

interface, making it an extremely difficult problem to model theoretically. Efficient simulations of a 3D drop must address the challenging issue of growing computational cost that scales on the order of $O(N^3)$, where N is the number of grid points along one dimension.

Fowler et al. proposed a simple movement pattern in parallel plate electrowetting devices to mix drops in air [FMK02]. Paik et al. [PPF03] studied the mixing performances of different movement patterns of aqueous drops in the same parallel-plate configuration but filled with silicone oil. We expect a fundamentally different flow pattern between a drop in air and a drop in oil, due to the significant viscosity difference of the external fluid. In addition, dye-based flow visualization must be considered with great care because the fluorescent dye creates a surface tension gradient, inducing a surface flow.

As a first step toward understanding the flow in a 3D drop actuated by electrowetting, we utilize micro particle image velocimetry (micro-PIV) [SWM98, MWS99] to characterize a small drop with moderate aspect ratio $\alpha = b/R \sim 1$. The drop is uniformly seeded with 2μm polystyrene beads, thus free of any surface tension gradient. We imaged the horizontal velocity fields on 7 planes of different heights from the bottom substrate. Using the continuity equation, we reconstruct the 3D velocity field from the 2D PIV experimental data. It is shown that a simple forward-and-back actuation strategy is inefficient for mixing purpose. We present some fundamental findings and build valuable insights that will help the design of new sophisticated electrowetting microfluidic devices.

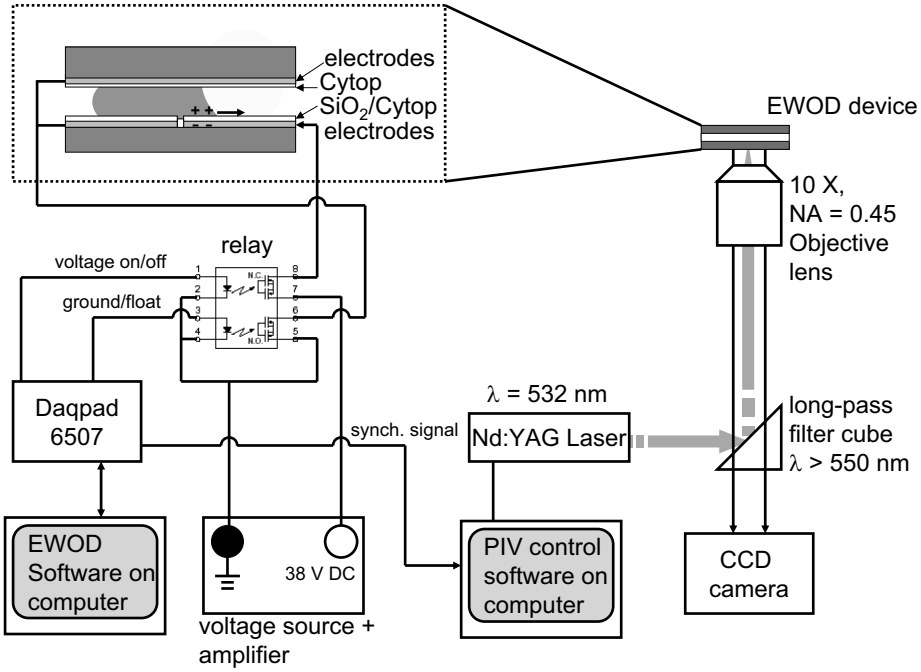

Figure 8.2: Electrowetting and PIV experimental setups.

8.1 Experimental setups and procedures

In collaboration with Professor Carl D. Meinhart, we conduct the experiment in the Microfluidics Laboratory in University of California, Santa Barbara (UCSB), where the micro-PIV equipment is located. The setup is illustrated in figure 8.2. The parallel-plate electrowetting devices are fabricated in the Micro and Nano Manufacturing Laboratory in University of California, Los Angeles (UCLA) using the Nanoelectronics Research Facility (Nanolab). The square shaped electrodes, each having 600μm ×600μm of area, are patterned on top of indium-tin oxide (ITO) coated glass wafers, which serves as the bottom substrates of the parallel-plate electrowetting devices. The remaining fabrication procedures are the same as the process flow outlined in chapter 2. The electrowetting device is completed by a pressure contact packaging developed

by Fan et al. [FK03]. The fluid used is deionized water seeded with Nile red colored fluorescent polystyrene microbeads of 2 μm diameter (Invitrogen) at 0.01% solid concentration. The resulting particle density is 2 $\times 10^7$ particles/mL. The user controls the applied potential on each electrode through a digital I/O board (Daqpad-6507, National Instrument) that controls electronic relays that pass the high voltage and the ground potential to the electrodes from the voltage source. The digital I/O board also sends a 5 V falling edge as the synchronization signal to the computer controlling the micro-PIV setup. The pulses of two frequency-doubled Nd:YAG lasers emitting green light (λ = 523 nm) are combined, directed through an optic fiber into a Nikon TE200 inverted microscope. The pulses are reflected by a long-pass filter cube onto the electrowetting device and illuminate the droplet through the transparent bottom substrate. The fluorescent emission is filtered by the long-pass filter cube and captured by a cooled 1030 $\times$ 1300 $\times$ 12 bit interline transfer CCD camera through a NA= 0.45, 10X objective lens, resulting $\sim$ 25μm of depth of focus.

During the experiment, 0.1 μl seeded fluid is deposited in the device, along with 6 larger droplets of deionized water, each with 5 μl in volume. An adhesive well made of SecureSeal (Grace BioLab) seals the device with the drops in it and maintains a substrate separation of approximately 388 μm. The moisture from the large water droplets saturates the moisture level in the device to prevent evaporation of the seeded drop. The seeded drop is constrained by the top and the bottom substrates and forms a disc with a diameter of approximately 800 μm. The device is then completed in the pressure contact packaging.

The experiment repeatedly actuates the drop back and forth between two electrodes as illustrated in figure (8.3). The drop initially sits on top of electrode B. At time t = 0, a 38 volts DC potential is applied on electrode A with electrode B grounded, and a synchronization signal is sent to the micro-PIV setup. At t = 150 ms, after

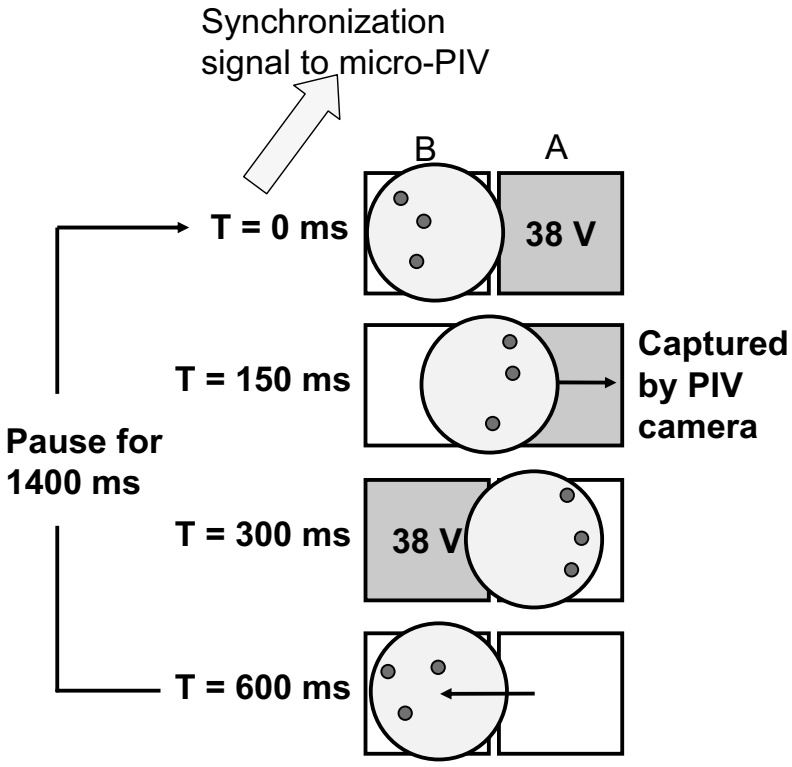

Figure 8.3: One cycle of actuation sequence of the electrowetting device.

receiving the synchronization signal, the micro-PIV setup fires the lasers and captures two images of the moving drop with 5-20 ms of delay between them. The waiting time t_w = 150ms is chosen so the droplet is moving at approximately midway between the two electrodes. At t = 300 ms, the actuation potential is switched onto electrode B for a duration of 300 ms with electrode A grounded to move the drop back to electrode B. Starting from t = 600 ms, both electrodes are grounded for 1400 ms before the next cycle of movement/image capture is initiated. Sixty sets of image pairs are captured in this manner. A sufficient time delay between the image pair must be chosen to resolve the lowest flow speed in the center of the drop. This indirectly influences the spatial resolution of the experiment, since maximum particle displacement must be sufficiently smaller than the size of the interrogation region used by the micro-PIV software [WGM01].We analyze the image pairs using interrogation regions of 96 pixels × 96 pixels, which yields 2-dimensional velocity data at 32μm ×32μm ×25μm resolution. As shown in table 8.1, we repeat the procedure on 7 planes of different heights, z, above the bottom substrate to obtain a stack of 2D velocity fields at t_w = 150ms. The 2D velocity field at different t_w are obtained for the height z = 148μm.

8.2 Results and discussion

Figure 8.4 shows the drop image captured by bright field microscopy with a 4X objective lens. The free interface shows up as a thick dark region surrounding the drop because the curvature of the interface interferes with the light scattering. Therefore we do not expect the micro-PIV to capture data in the region near the interface.

Figure 8.5a shows the 2D lagrangian velocity field and the streamlines at height z = 148μm. The speed of the droplet (i.e. the speed of the moving reference frame) is approximately 2 mm/s. Due to the lack of data near the interface, the streamline produced by the velocity field terminates there as expected. The 2D data clearly shows

height z (μm)	delay time t_w (ms)
52	150
100	150
148	40 80 150 180 210 240 280
196	150
244	150
292	150
340	150

Table 8.1: The heights above the bottom substrate and the time delays used to capture 2-dimensional velocity field.

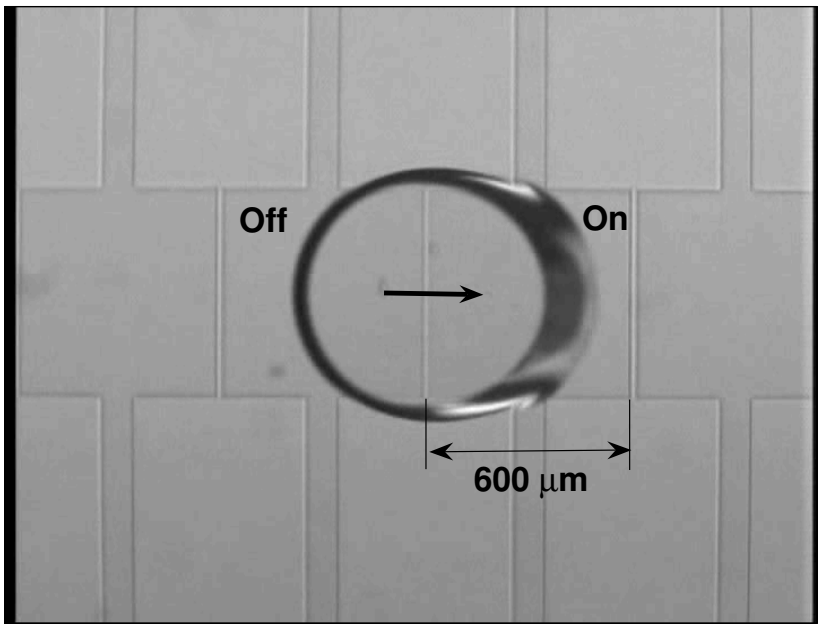

Figure 8.4: Bright field image of the moving drop.

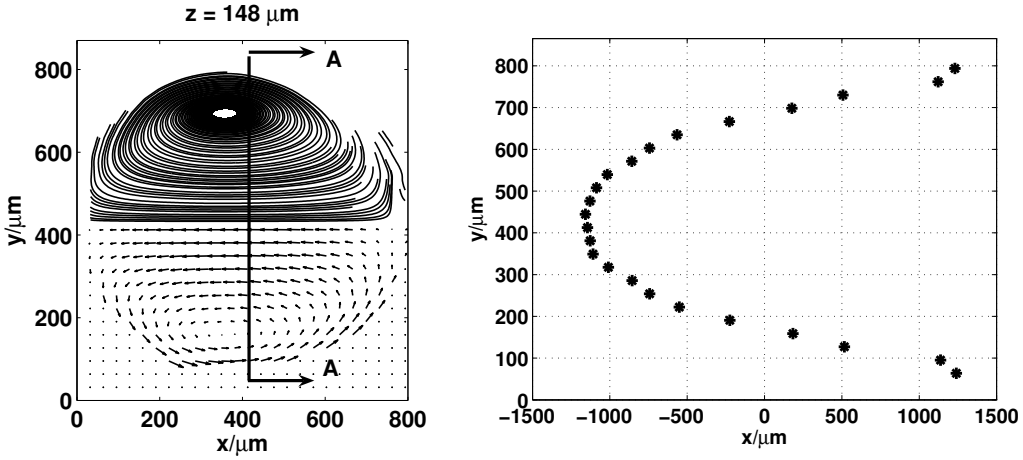

(a) (b)

Figure 8.5: (a) 2-dimensional velocity field at $z = 148\mu$m (bottom half) and the streamlines (top half). (b) the axial velocity component, u, at cross-section AA. ($y = 416\mu$m).

two internal circulations symmetric about the moving axis of the drop, **x**. Figure 8.5b shows a smooth variation of the axial velocity component along the cross-section of the 2D plane at $y = 426\mu$m. The fluid flows forward along the air-liquid interface of the drop toward the nose and circulates backward near the center, a flow pattern similar to the one reported by Fowler et al. [FMK02].

We compute the 2-dimensional vorticity by finite difference at each data point,

$$\eta_{i,j} = \frac{\partial v_{i,j}}{\partial x} - \frac{\partial u_{i,j}}{\partial y}, \tag{8.2}$$

Figure 8.6 shows the contour plot of the vorticity generated by the two circulations at $t_w = 150$ ms. Significant vorticity for mixing process are generated on the two sides of the drop near the air-liquid interface. To further enhance mixing, the drop actuation must break the symmetry of the circulating flow. One strategy is to actuate the drop through a sequence of movements in different directions. An example of the concept is the square movement sequence proposed by Fowler et al. [FMK02]), as illustrated in figure 8.7. The movement sequence generates 4 pairs of vortices within the drop.

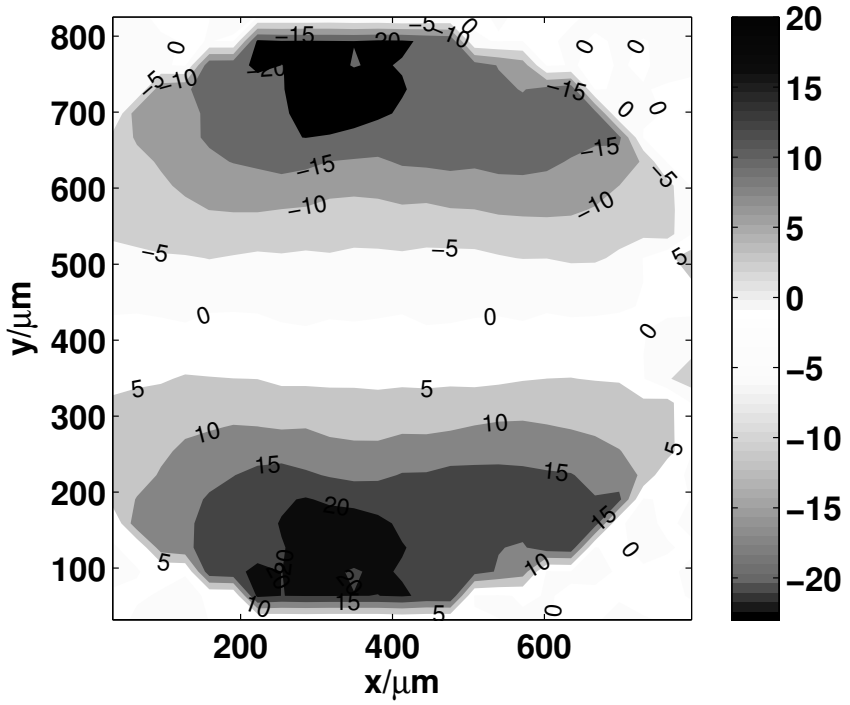

Figure 8.6: Contour plot of the vorticity in the horizontal plane at $z = 148\mu$m.

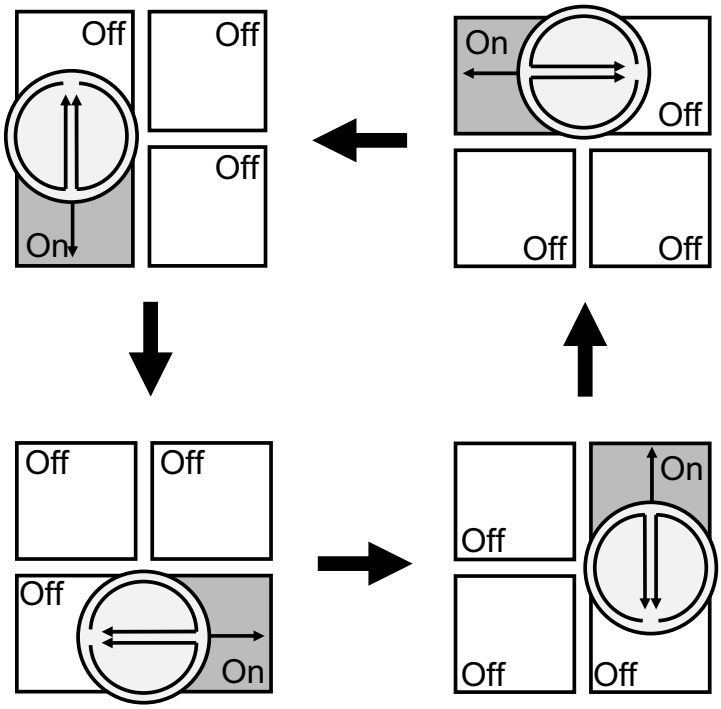

Figure 8.7: A drop moving through a square movement pattern. Adopted from Fowler et al. [FMK02].

The dynamics can be modeled as a blinking vortex flow, a sequence of vortices turning on and off periodically at different locations [Are84], making the flow in the drop a chaotic system [Ott89].

To get a better idea of the relation between vorticity and the drop speed, we compute the mean velocity, at different t_w, on the horizontal plane $z = 148\mu$m. Integrating the velocity over time gives us an estimate of the drop displacement. For a droplet of 800 mm in disc diameter moving on electrodes of 600μm in length, the nose of the droplet already extends approximately 200μm into electrode A at the beginning of each capture sequence. Since the droplet stretches into an elliptical shape, we expect less than 400μm of distance for the droplet to travel. Figure 8.8a shows the drop moves steadily at a speed of $\sim$ 2 mm/s before slowing down as its nose approaches the far

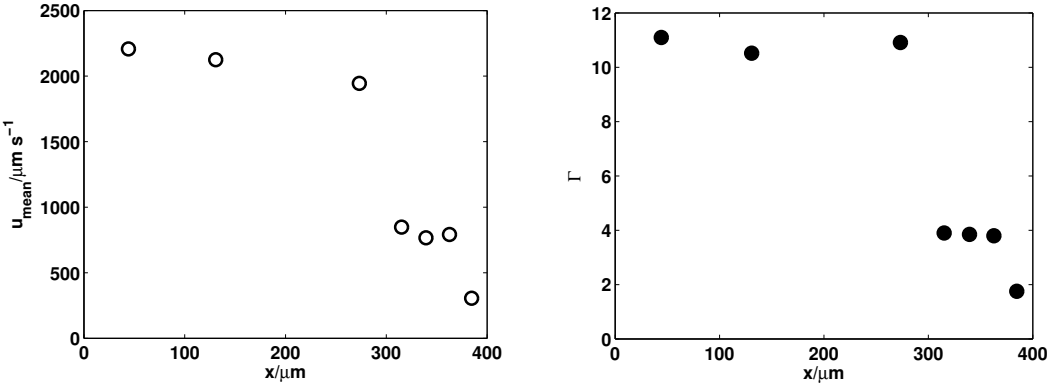

(a) (b)

Figure 8.8: (a) Mean velocity of the drop at different locations. (b) Circulation strength of the flow at different locations.

edge of electrode A. The steady movement is sustained for approximately 150 ms before the drop slows down. To relate the circulation of vortices to the drop motion, we sum over the entire plane the absolute value of the vorticity,

$$\Gamma = \sum_{i,j=1}^{N} |\eta_{i,j}|, \tag{8.3}$$

to estimate the strength of the circulation as shown in figure 8.8b. Comparing the velocity and the circulation strength shows a close corresponds between the two flow properties.

We compare the previous strategy of generating chaotic mixing (figure 8.7) with the simple, forward-and-back mixing strategy shown in figure 8.3. We compute the overall displacements of the fluid in one cycle of forward-and-back drop motion by comparing the positions of the tracer particles between the first images from all 60 image pairs. Figure 8.9 compares the instantaneous velocity field at t_w = 150 ms and the overall displacement field of the particles on the horizontal plane at z = 148μm. The overall displacement field shown in figure 8.9b is symmetric about the moving axis,

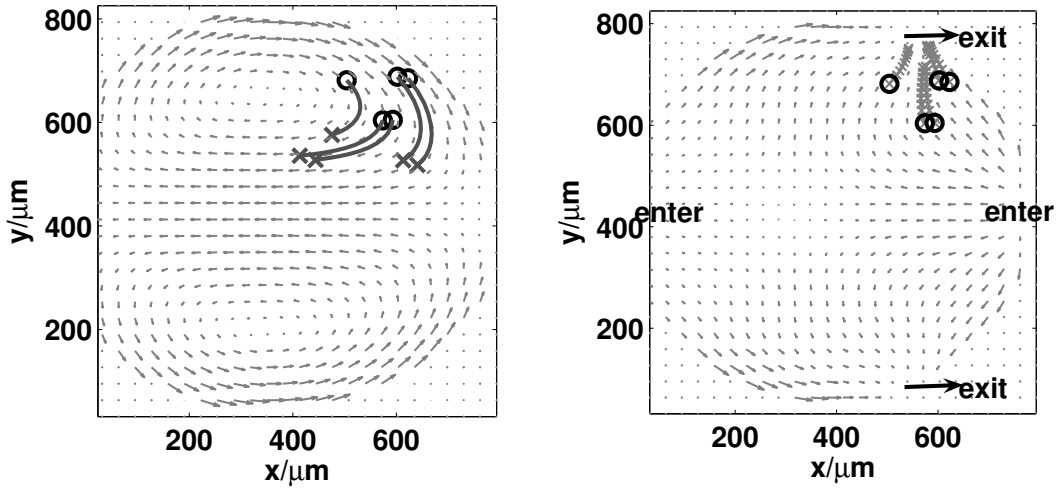

(a) (b)

Figure 8.9: The displacement of particles starting at random positions denoted by ◯s (a)The instantaneous velocity field at t_w = 150 ms and z = 148μm. ×s denote the particle positions after 150 ms of convection by the instantaneous velocity field; (b) The overall displacement field at z = 148μm by the forward-and-back actuation. The flow enters the z plane near the nose and the tail of the droplet and exits out of the plane near the front half of the meniscus. ×s denote the ending positions of each cycle.

x. The field shows the fluid entering the horizontal plane near the nose (x = 800μm) and the tail of the drop (x = 0μm). The flow converges toward two points near the front half of the drop interface, where it exits in the z-direction out of the horizontal plane. Since the flow in the drop is unsteady, the direction of the displacement field does not necessary follow the direction of the instantaneous velocity field. Integrating the displacements of tracer particles from random initial positions for 150 ms (figure 8.9a) shows that the Lagrangian velocity field of the forward drop motion convects the particles over a long distance (∼ 100μm). In contrast, the net displacements after one cycle of drop actuation are much shorter (∼ 10μm) in different directions. This indi-

cates the reverse drop motion returns the particles back to near their initial positions, a reversible characteristic of a well-ordered laminar flow. As figure 8.9b shows, transporting the particles over a significant distance (> 100μm) requires 15 cycles of drop actuations. This indicates the forward-and-back motion is inefficient for drop mixing, even if one considers dye with higher diffusion coefficient.

For a 3D drop, it is also important to understand how the fluid is circulating in the direction normal to the substrates. To obtain the velocity component normal to the substrates, w, we first compute the 2D divergence of the horizontal velocity measured on all 7 horizontal planes. Using the continuity equation, the normal gradient of w is

$$\frac{\partial w}{\partial z} = -\left(\frac{\partial u}{\partial x} + \frac{\partial v}{\partial y}\right). \tag{8.4}$$

We do not have the data at the interface due to the interference from the curving air-liquid interface. Therefore, we restrict our attention to the bulk of the drop, where the data on all 7 planes are available. Since the aspect ratio of the drop, b/R, is close to 1, we expect the bulk flow to be 3D as well. We first interpolate a 7th order polynomial, $p(z)$ through the data of $\partial w/\partial z$ through all 7 planes,

$$p\,(z) = \sum_{n=1}^{7} c_n z^n \tag{8.5}$$

with no-slip boundary condition at $z = 388$μm. The no-slip boundary condition at $z = 0$μm is automatically satisfied by the interpolation function we choose. Subsequently integrating $p(z)$ give us the an estimate of the normal velocity component. The 3D velocity field is shown in figure 8.10. Indeed, we observe 3D flows in the bulk of the drop. The flow gains significant normal velocity component as it approaches the drop interface. A strong downward flow due to the electrowetting from the bottom substrate is observed near the nose of the drop. The fluid near the substrates circulates back into the drop near the rear of the drop. In figure 8.2, the vertical cross sections shows that the flow profile is asymmetric across the height of the drop due to the cor-

responding asymmetric actuation in the current electrowetting devices. The significant recirculation in a thick drop suggests that the 3D flow stretches and folds the material interface across the height of the drop. This flow behavior reduces the striation length and enhances mixing, as analyzed by Handique et al. [HB00] for slit-type channel. An extension of the analysis beyond the assumption of the fully developed parabolic flow profile is needed to analyze a thick 3D droplet.

We characterized the internal flow of a thick droplet actuated by electrowetting using the micro-PIV technique. The experimental finding shows the flow in a 3D droplet deviates from the parabolic flow profile used in current flow simulations. Significant recirculation is observed near the droplet interface, which neglected by the 2D reduction of the Navier-Stokes equation. To further our understanding of the fluid dynamics, it is necessary to address the challenges of modeling and simulating a constrained 3D droplet with a free air-liquid interface. Our 2D data shows two symmetric circulations within the moving droplet. Due to the reversibility of the flow, a simple forward-and-back motion is inefficient for mixing. Effective mixing has to be accomplished through designing irreversible movement patterns to break the symmetry of the symmetric circulating flow in the horizontal plane. One strategy is to construct a blinking vortex map by composing droplet movement through a sequence of alternate directions such as the one proposed by Fowler et al. [FMK02]. It has been shown that the mixing efficiency of the blinking vortex flow is dependent on the flow strength, ψ [KRO87]. In the context of the square movement pattern proposed by Fowler et al. [FMK02] the flow strength is defined by

$$\psi = \frac{\Gamma T}{2\pi a} \tag{8.6}$$

where Γ is the strength of the vortex, T is the period of the alternate actuations and a is the distance between the vortices. Khakhar et al. [KRO87] shows numerically that optimal mixing efficiency is achieved when $\psi = 0.8$. Our results show that the vortex

strength is related to the mean speed of the droplet, U, which is related to the actuation voltage [LGB07]. The period of the alternate actuation is also related to the speed of the droplet by L/U, where L is is the length of the electrodes. The distance between the vortices is related to the drop diameter. All three physical parameters are controllable by the actuation voltage, the device geometry, and the drop size. Therefore, the mixing efficiency by a movement pattern can be further improved by tuning these design parameters to achieve the optimal flow strength. It will be interesting to further explore the relationship of these physical parameters to optimize the electrowetting actuation for mixing purpose.

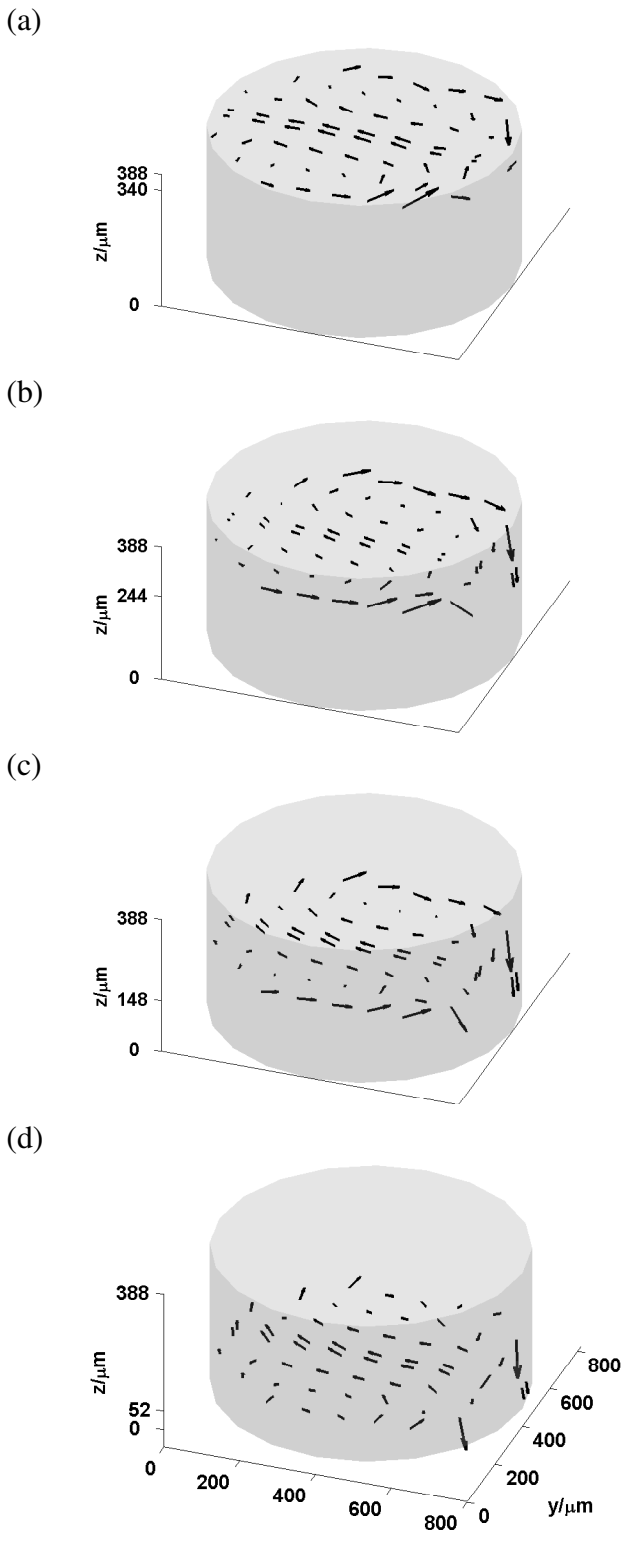

Figure 8.10: The 3-dimensional velocity field at (a) $z = 340\mu m$, (b) $z = 244\mu m$, (c) $z = 148\mu m$, and (d) $z = 52\mu m$.

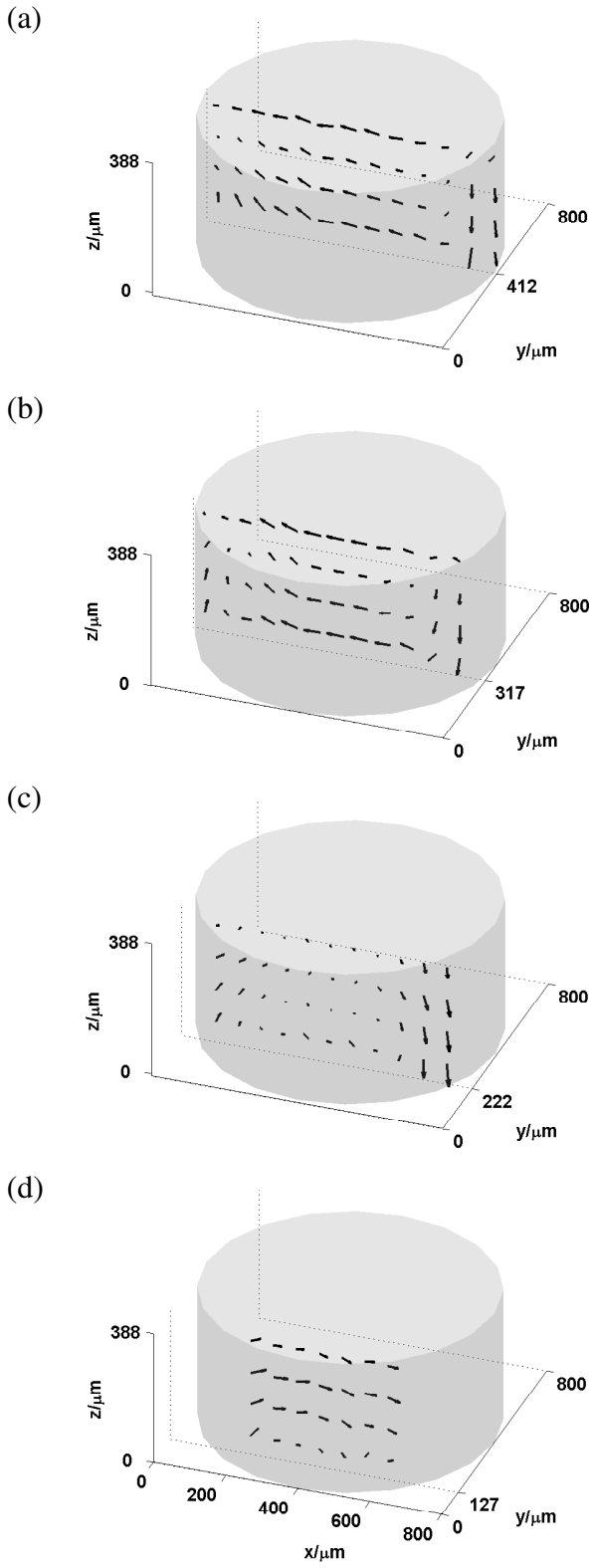

Table 8.2: The 3-dimensional velocity field at (a) y = 412μm, (b) y = 317μm, (c) y = 222μm, and (d) y = 127μm.

CHAPTER 9

Conclusions and future researches

This thesis presents the research into the fluid dynamics of a liquid drop in air actuated by electrowetting, especially EWOD. In the limit of a thin flat drop, we studied a diffuse interface description of the drops in a Hele-Shaw cell in the form of a degenerate Cahn-Hilliard equation with a spatially varying surface energy. Through matching asymptotic expansions, we show that the phase field approach approximates the sharp interface Hele-Shaw flow in the limit of small diffuse interface thickness. The dynamics in the sharp interface limit is validated numerically by a direct comparison to the boundary integral methods. This approach enables us to naturally simulate the macroscopic dynamics of drop splitting, merging, and translation under the influence of local electrowetting.

In order to efficiently simulate the Cahn-Hilliard equation, we utilized a biharmonic modified time-stepping scheme to solve the forth order nonlinear equation. In addition to the Cahn-Hilliard equation, we demonstrated the applicability of the algorithm on other equations for thin film flows and spinodal decomposition in binary alloys. Solving the Cahn-Hilliard using an explicit time-stepping is restricted by a stiff constraint of $O(\Delta t^4)$. The biharmonic modified scheme allows us to relax the constraint tremendously while preserving the monotonic energy dissipation property. However, such gain must be balanced with the requirement of numerical accuracy. We quantified the numerical accuracy and developed an estimate as a tool for diagnosing the programming.

As illustrated by the reduced order model, the contact line dynamics significantly affects the problem by modifying the cross substrate of the interface. Based on the measured advancing and receding contact angles, we showed that the strong influence of contact line dynamics accounts for up to a four fold increase in the dynamic timescale of the Hele-Shaw approximation. This points out that using Lippman equation under the assumption of quasi-steady interfacial motion is not adequate to capture the physics at the interface of the electrowetting drop. Knowledge of the interface geometries near the electrowetting boundary may provide improvement to our estimate. Numerical simulations of drop motions showed a range of dynamic timescale that is consistent with the experimentally measured timescale.

The assumption of constant advancing and receding contact angles in the reduced order model is obviously a crude approximation. Improvements to this approximation need to account for the dynamically varying contact angles since the normal velocity of the entire drop interface varies. Careful characterizations of the electrowetting contact line dynamics and asymptotic matching to the bulk Hele-Shaw flow must be considered to determine an appropriate pressure boundary condition. In short, this will introduce velocity dependence in the formulation of $B(\omega, Ca|_{\partial\Omega})$ in equation (3.12), where $Ca|_{\partial\Omega}$ is the local capillary number of the interface. To formulate $B(\omega, Ca|_{\partial\Omega})$, the asymptotic analysis of Weinstein et al. [WDU90] must be extended from the special case of a travelling wave solution to the general motion of a Hele-Shaw drop. Doing so presents an interesting problem for future research.

Improvements to the constant contact angle approximation need to account for the dynamically varying contact angle since the normal velocity of the entire drop interface varies. The empirically derived power law of $\theta \sim Ca^{1/3}$ have been widely accepted [Tan79, Ber93, deG85]. This introduces a velocity dependence in the formulation of the capillary pressure, $B(\omega, Ca|_{\partial\Omega})$ in equation (3.12), where $Ca|_{\partial\Omega}$ is the local capillary

number of the interface. Numerically resolving the sharp interface motion adds another complexity to the simulation of the sharp interface model. Interestingly, the coupling between pressure boundary condition and the local contact line velocity can be accomplished by modifying equations (4.7-4.8) to a viscous degenerate Cahn-Hilliard equation [Sep96]. As an example, consider the addition of another time dependent term.

$$\epsilon\rho_t + \epsilon^2\nabla\cdot(\rho\nabla\ (\rho_t)) = \nabla\cdot(\rho\nabla(\delta E)), \tag{9.1}$$

$$\delta E = \frac{A}{\gamma}\left(-\epsilon^2\triangle\rho + g'(\rho)\right) - \epsilon\omega, \tag{9.2}$$

A matched asymptotic expansion similar to the one in section 4.2 shows the addition of $\nabla\cdot(\rho\nabla\rho_t)$ introduces a linear contact line velocity dependence into the pressure boundary condition. The linear velocity dependence of the capillary pressure is equivalent to the linear dynamic contact angle model of Weinstein et al. [WDU90]. In contrast to Weinstein et al., the viscous Cahn-Hilliard equation incorporates the velocity of the local contact line, instead of the steady state drop velocity. Further work is required to extend the formulation to couple the capillary pressure to a nonlinear velocity term. The additional nonlinearity in equation (9.1) changes the properties of the numerical approximation dramatically and warrants new numerical research efforts to efficiently solve this equation.

The threshold voltage for moving a drop shown in figure 2.4 indicates hysteresis may also be a significant source of dissipation. The MEMS fabrication process for the electrowetting devices produces variations of the surface energy that must be overcome by the moving contact line. The dissipation becomes more significant as the drop radius decreases, such as in microfluidic applications. Even with the length scale of our experiment ($\sim$ 1cm), the surface effect may become important for specific motions such as the splitting of a partially wetting drop. A preliminary study shows the neck width at pinch-off is much smaller than the separation height, b. This behavior

is different from experiments mentioned by Constantin et al. [CDG93], suggesting the surface effect may delay the capillary pinch-off by preventing the fluid neck from separating off the substrates. For a drop in motion, the linear relationship of the drop velocity in figure 2.4 suggests the dissipation by the contact angle hysteresis can be accounted by an offset of the square of the voltage. However, the range of linear behavior is not sufficient to validate this hypothesis. To further study the effect of hysteresis on the timescale of motion, additional microscopic experiments are needed to characterize the strength and the uniformity of the defects on the substrates. This information will allow us to introduce a macroscopic model of the microscopic physics, such as the work of Joanny et al. [JR90], into the study of electrowetting drops.

In the limit of a thick drop actuated by electrowetting, we utilized the micro-PIV to investigate its flow field. The 3D flow field shows significant deviation from the parabolic flow profile used in the flow model for a thin flat drop. Significant recirculation is observed near the drop interface. The 2D data in the horizontal planes parallel to the substrate shows two symmetric circulations within the moving drop as predicted by Fowler et al. [FMK02]. The observation of this flow pattern validates the concept of generating chaotic mixing within a drop by composing the drop movement by electrowetting through a sequence of different directions. The flow generated by the actuation sequence can be treated as a blinking vortex flow. The mixing performance of such a flow can be related to various geometric and actuation parameters of the electrowetting device. It is beneficial to further characterize the flow properties to these physical parameters so an optimization of the electrowetting device for mixing purpose can be conducted.

Another interesting problem is the theoretical modelling of a viscous drop of larger aspect ratio. In this case, the 2D Hele-Shaw model can no longer provide adequate approximation. On the other hand, a full three-dimensional simulation of such a drop

is complicated by the coupling of the no-slip boundary condition on the solid surfaces with the stress-free interfacial condition on the air-liquid interfaces. In addition, the computational cost of such a simulation grows on the order of $O(N^3)$, making fast simulation a challenging issue. It would be desirable to develop a reduced dimension model that is computationally tractable while preserving the essential information about the velocity component normal to the substrates. Galerkin methods from numerical analysis may provide an interesting direction to accomplish this [Egg96, HD98, WBH03].

APPENDIX A

Modified Equation

Consider the finite difference approximation of the nonlinear diffusion (5.7) in one dimension.

$$\frac{u_i^{n+1} - u_i^n}{\Delta t} + M\left(\delta_{xxxx}u^{n+1} - \delta_{xxxx}u^n\right) = -\delta_x\left(u_i^n \delta_x \delta_{xx} u_i^n\right), \tag{A.1}$$

where common central difference operators are used to simplify the formula.

$$\begin{aligned}
\delta_x u_i &= \left(u_{i+1/2} - u_{i-1/2}\right)/\Delta x, \\
\delta_x \delta_{xx} u_{i+1/2} &= \left(u_{i+2} - 3u_{i+1} + 3u_i - u_{i-1}\right)/\Delta x^3, \\
\delta_{xxxx} u_i &= \left(u_{i+2} - 4u_{i+1} + 6u_i - 4u_{i-1} + u_{i-2}\right)/\Delta.x^4.
\end{aligned}$$

Expanding each terms in the difference equation by Taylor series gives

$$\begin{aligned}
\frac{u_i^{n+1} - u_i^n}{\Delta t} &= u_t + \frac{\Delta t}{2} u_{tt} + O\left(\Delta t^2\right), \\
\delta_x\left(u_i^n \delta_x \delta_x x u_i^n\right) &= \left(u u_{xxx}\right) + O\left(\Delta x^2\right), \\
\delta_{xxxx} u^{n+1} - \delta_{xxxx} u^n &= \Delta t u_{xxxxt} + O\left(\Delta t \Delta x^2\right).
\end{aligned}$$

Substitute back into the difference equation results the modified equation

$$u_t + \left(u u_{xxx}\right)_x = -\frac{\Delta t}{2} u_{tt} - M \Delta t u_{xxxxt} + O\left(\Delta x^2 + \Delta t^2\right). \tag{A.2}$$

Defining $\mathcal{F}(u) = u u_{xxx}$, we use the fact that $u_t = -\mathcal{F}_x + O(\Delta t + \Delta x^2)$ to remove the time derivatives on the left hand side of (A.2)

$$u_t + \left(\mathcal{F}(u)\right)_x = -\Delta t\left[\left(\frac{\partial \mathcal{F}}{\partial u}\left(\mathcal{F}(u)\right)_x\right)_x - M\left(\mathcal{F}(u)\right)_{xxxxx}\right] + O\left(\Delta x^2 + \Delta t^2\right) \tag{A.3}$$

APPENDIX B

Higher order expansion of the pressure boundary condition

The perturbation expansion described in 7.2 can be carried to the next order, $O(1)$. The normal stress boundary condition in this order is

$$P^1|_{\partial\Omega} = \left[\frac{-h_r^1}{\left(1+(h_x^0)^2\right)^{\frac{3}{2}}}\right]_r - \frac{h_r^0}{\left(1+(h_x^0)^2\right)^{\frac{1}{2}}} \tag{B.1}$$

Integrating this equation with the boundary conditions $h_r^1(R) = 0$, $h^1(R) = 0$ and $h^1(r') = 0$ gives

$$P^1|_{\partial\Omega} = -\frac{1+\sin\theta_s}{\cos\theta_s}\left(\frac{\theta_s}{2} - \frac{\pi}{4}\right) + O(\alpha), \tag{B.2}$$

for the symmetric receding interface. Inspection of the $O(1)$ term, plotted in figure B.1b, shows A in equation (3.5 varies between a maximum of 1 when $\theta_s = \pi/2$ and a minimum of $\pi/4$ when $\theta_s = 0$ and π.

For the non-symmetric interface in the electrowetting region, the boundary condition is

$$P^1|_{\partial\Omega} = -\frac{\cos\theta_t}{2\left(1-\cos\left(\theta_b-\theta_t\right)\right)}\left(\frac{\cos\theta_b}{\cos\theta_t}\sin\left(\theta_b-\theta_t\right) + \theta_t - \theta_b\right) + O(\alpha). \tag{B.3}$$

For the interface inside of the electrowetting region, figure B.1a shows A varying between a maximum value of 1.0 when $\theta_b = \theta_t = \pi/2$ and a minimum of 0.5 at $\theta_b = 0$ and $\theta_t = \pi/2$. Since relaxation dominates away from the boundary of the

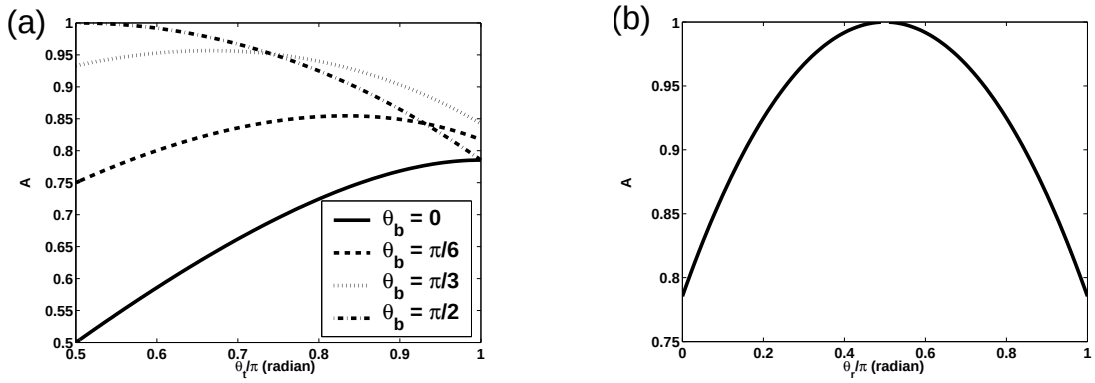

Figure B.1: Horizontal curvature A for (a) electrowetting and (b) non-electrowetting menisci.

electrowetting region, we can obtain good estimate of A by substituting the data in figure 2.6. The computed values of A are 0.9994 and 0.9831 for the interfaces outside and inside of the electrowetting region respectively. This supports the use of $A = 1$.

References

[AKK06] J. Aizenberg, T. Krupenkin, and P. Kolodner. "Accelerated chemical reactions for lab-on-a-chip applications using electrowetting induced droplet self oscillations." In *Mater. Res. Soc. Symp. Proc.*, volume 915, pp. 103–111. MRS, 2006.

[Are84] H. Aref. "Stirring by chaotic advection." *J. Fluid Mech.*, **143**:1–21, 1984.

[BBG99] J. W. Barrett, J. F. Blowey, and H. Garcke. "Finite element approximation of the Cahn-Hilliard equation with degerate mobility." *SIAM J. Numer. Anal.*, **37**:286–318, 1999.

[BCM07] F. Bottausci, C. Cardonne, I. Mezic, and C. D. Meinhart. "An Ultrashort Mixing Length Micromixer: The Shear Superposition Micromixer." *Lab on a Chip*, **7**:396–398, 2007.

[Ber93] J. C. Berg, editor. *Wettability*. Marcel Dekker, New York, 1993.

[BKL86] D. Bensimon, L. P. Kadanoff, S. Liang, and S. Shraiman. "Viscous flow in two dimensions." *Rev. Mod. Phys.*, **58**:977–999, 1986.

[Bra94] A. J. Bray. "Theory of phase-ordering kinetics." *Adv. Phys.*, **43**:357–524, 1994.

[Bre61] F. P. Bretherton. "The motion of long bubble in tubes." *J. Fluid Mech.*, **10**:166–188, 1961.

[CDG93] P. Constantin, T. F. Dupont, R. E. Goldstein, L. P. Kadanoff, M. J. Shelley, and S.-M. Zhou. "Droplet breakup in a model of the Hele-Shaw cell." *Phys. Rev. E*, **47**:4169–4181, 1993.

[CF88] G. Caginalp and P. Fife. "Dynamics of layered interfaces arising from phase boundaries." *SIAM J. Appl. Math.*, **48**:506–518, 1988.

[CMF01] S. K. Cho, H. Moon, J. Fowler, S.-K. Fan, and C.-J. Kim. "Splitting a Liquid Droplet for Electrowetting-Based Microfluidics." In *Proc. ASME IMECE*, pp. Pap. 2001–23831, New York, NY, 2001.

[CMK03] S.-K. Cho, H. Moon, and C.-J. Kim. "Creating, transporting, cutting, and merging liquid droplets by electrowetting-based actuation for digital microfluidic circuits." *J. Microelectromech. Syst.*, **12**:70–80, 2003.

[CSO99] L. Carrillo, J. Soriano, and J. Ortin. "Radial displacement of a fluid annulus in a rotating Hele-Shaw cell." *Phys. Fluids*, **11**:778–785, 1999.

[CSO00] L. Carrillo, J. Soriano, and J. Ortin. "Interfacial instabilities of a fluid annulus in a rotating Hele-Shaw cell." *Phys. Fluids*, **12**:1685–1698, 2000.

[CTD05] J. Z. Chen, S. M. Troian, A. A. Darhuber, and S. Wagner. "Effect of contact angle hysteresis on thermocapillary droplet actuation." *J. Appl. Phys.*, **97**:014906, 2005.

[deG85] P. G. deGennes. "Wetting: statics and dynamics." *Rev. Mod. Phys.*, **57**:827–863, 1985.

[DKB00] J. A. Diez, L. Kondic, and A. Bertozzi. "Global models for moving contact lines." *Phys. Rev. E*, **63**:179–206, 2000.

[DSW03] S. Devasenathipathy, J. G. Santiago, S. T. Wereley, C. D. Meinhart, and K. Takehara. "Particle imaging techniques for microfabricated fluidic systems." *Exp. in Fluids*, **34**:504–513, 2003.

[DT05] A. Darhuber and S. M. Troian. "Principles of microfluidic actuation by manipulation of surface stresses." *Annu. Rev. Fluid Mech.*, **37**:425–455, 2005.

[Dus79] E. B. Dussan. "On the spreading of liquid on solid surfaces: static and dynamic contact lines." *Ann. Rev. Fluid Mech.*, **11**:371–400, 1979.

[Egg96] J. Egger. "Nonlinear dynamics and breakup of free-surface flows." *Rev. Mod. Phys.*, **69**:865–929, 1996.

[Fai07] R. B. Fair. "Digital microfluidics: is a true lab-on-a-chip possible?" *Microfluid. Nanofluid.*, **3**:245–281, 2007.

[Fan03] S. K. Fan. *Digital Microfluidics by Cross-reference EWOD Actuation: Principle, Device & System*. PhD thesis, University of California, Los Angeles, 2003.

[FB97] R. Ferreira and F. Bernis. "Source-type solutions to thin-film equations in higher dimensions." *Euro. J. Appl. Math.*, **9**:507–524, 1997.

[FK03] S.-K. Fan and C. Hashi C.-J. Kim. "Manipulation of multiple droplets on nxm grid by cross-reference EWOD driving scheme and pressure-contact packaging." In *Proc. IEEE Conf. Micro Electro Mechanical Systems, Kyoto, Japan*, pp. 694–697. IEEE, 2003.

[FMK02] J. Fowler, H. Moon, and C.-J. Kim. "Enhancement of Mixing by Droplet-Based Microfluidics." In *Proc. IEEE Conf. Micro Electro Mechanical Systems, Las Vegas, U.S.A*, pp. 97–100. IEEE, 2002.

[FN94] M. L. Ford and A. Nadim. "Thermocapillary migration of an attached drop on a solid surface." *Phys. Fluids*, **6**:3183–3185, 1994.

[Fre03] J. B. Freund. "The atomic detail of a wetting/dewetting flow." *Phys. Fluids*, **15**:L33–L36, 2003.

[Gla01] K. Glasner. "Nonlinear preconditioning for diffuse interfaces." *J. Comp. Phys.*, **174**:695–711, 2001.

[Gla03] K. Glasner. "A diffuse interface approach to Hele-Shaw flow." *Nonlinearity*, **16**:49–66, 2003.

[GR00] G. Grun and M. Rumpf. "Nonnegativity preserving convergent schemes for the thin film equation." *Numer. Math.*, **87**:113–152, 2000.

[Gre78] H. P. Greenspan. "On the motion of a small viscous droplet that wets a surface." *J. Fluid Mech.*, **84**:125–143, 1978.

[Had99] N. G. Hadjiconstantinou. "Hybrid atomistic-continuum formulations and the moving contact line problem." *J. Comp. Phys.*, **154**:245–265, 1999.

[HB00] H. Handique and M. A. Burns. "Mathematical modeling of drop mixing in a slit-type microchannel." *J. Micromech. Microeng.*, **11**:548–554, 2000.

[HD98] A. E. Hosoi and T. F. Dupont. "Some reduced dimension models based on numerical methods." In J. W. Jerome, editor, *Modelling and Computation for Applications in Mathematics, Science and Engineering*, pp. 59–80. Oxford University Press, New York, 1998.

[Hel98] H. J. S. Hele-Shaw. "The flow of water." *Nature*, **58**:34–36, 1898.

[HF03] R. A. Hayes and B. J. Feenstra. "Video-speed electronic paper based on electrowetting." *Nature*, **425**:383–385, 2003.

[HLS94] T. Hou, J. S. Lowengrub, and M. J. Shelly. "Removing the stiffness from interfacial flow with surface-tension." *J. Comp. Phys.*, **114**:312–338, 1994.

[Hoc77] L. M. Hocking. "A moving fluid interface. part 2. the removal of the force singularity bu a slip flow." *J. Fluid Mech.*, **79**:209–229, 1977.

[Hom87] G. M. Homsy. "Viscous fingering in porous media." *Ann. Rev. Fluid Mech.*, **19**:271–311, 1987.

[How92] S. D. Howison. "Complex variable methods in Hele-Shaw moving boundary problems." *Eur. J. Appl. Maths*, **3**:209–224, 1992.

[HS71] C. Huh and L. E. Scriven. "Hydrodynamic model of steady movement of a solid-liquid-fluid contact line." *J. Coll. Int. Sci.*, **35**:85–101, 1971.

[Jac00] D. Jacqmin. "Contact-line dynamics of a diffuse fluid interface." *J. Fluid Mech.*, **402**:57–88, 2000.

[JR90] J-F. Joanny and M. Robbins. "Motion of a contact line on a heterogenous surface." *J. Chem. Phys.*, **92**:3206–3212, 1990.

[Kan02] K. H. Kang. "How electrostatic fields change contact Angle in electrowetting." *Langmuir*, **18**:10318–10322, 2002.

[KH88] A. R. Kopfsill and G. M. Homsy. "Bubble motion in a Hele-Shaw cell." *Phys. Fluids*, **31**:18–26, 1988.

[Kim99] C.-J. Kim. "MEMS Devices Based on the Use of Surface Tension." In *Int. Semiconductor Device Research Symposium (ISDRS 99), Charlottesville, VA, U.S.A*, pp. 481–484, Dec. 1999.

[Kim00] C.-J. Kim. "Microfluidics Using the Surface Tension Force in Microscale." In *SPIE Symp. Micromachining and Microfabrication*, volume 4177, pp. 49–55, Santa Clara, CA, 2000.

[KO97] R. V. Kohn and F. Otto. "Small surface energy, coarse-graining, and selection of microstructure." *Physica* D, **107**:272–289, 1997.

[KRO87] D. V. Khakhar, H. Rising, and J. M. Ottino. "analysis of chaotic mixing in two chaotic flows." *J. Fluid Mech.*, **172**:419–451, 1987.

[LGB07] H.-W. Lu, K. Glasner, A. L. Bertozzi, and C.-J. Kim. "Electrowetting in a Hele-Shaw Cell." *J. Fluid Mech.*, **590**:411–435, 2007.

[Lip75] M. G. Lippman. "Relations entre les phènoménes électriques et capillaires." *Ann. Chim. Phys.*, **5**:494–548, 1875.

[LK98] J. Lee and C.-J. Kim. "Liquid Micromotor Driven by Continuous Electrowetting." In *IEEE Micro ElectroMechanical Systems Workshop*, pp. 538–543, Heidelberg, Germany, 1998.

[LL87] T. S. Light and S. L. Licht. "Conductivity and resistivity of water from the melting to critical point." *Anal. Chem.*, **59**:2327–2330, 1987.

[LLG02] H. Lee, J. S. Lowengrub, and J. Goodman. "Modeling pinchoff and reconnection in a Hele-Shaw cell. I. The models and their calibration." *Phys. Fluids*, **14**:492–513, 2002.

[LMF01] J. Lee, H. Moon, J. Fowler, J. Schoellhammer, and C.-J. Kim. "Addressable Micro Liquid handling by Electric Control of Surface Tension." In *Proc. IEEE Conf. Micro ElectroMechanical Systems*, pp. 499–502, Interlaken, Switzerland, 2001.

[LMF02] J. Lee, H. Moon, J. Fowler, J. Schoellhammer, and C.-J. Kim. "Electrowetting and electrowetting-on-dielectric for microscale liquid handling." *Sensors and Actuators* A, **95**:259–268, 2002.

[LSS00] R.-H. Liu, M. A. Stremler, K. V. Sharp, M. G. Olsen, J. G. Santiago, R. J. Adrian, H. Aref, and D. J. Beebe. "Passive mixing in a three-dimensional serpentine microchannel." *J. Microelectromech. Syst.*, **9**:190–197, 2000.

[LST07] Y.-K. Lee, C. Shih, P. Tabeling, and C.-M. Ho. "Experimental study and nonlinear dynamic analysis of time-periodic micro chaotic mixers." *J. Fluid Mech.*, **575**:425–448, 2007.

[MB05] M. Mugele and J-C. Baret. "Electrowetting: from basics to applications." *J. Phys.: Condens. Matter*, **17**:R705–R774, 2005.

[MBS06] F. Mugele, J. C. Baret, and D. Steinhauser. "Microfluidic mixing through electrowetting-induced droplet oscillations." *Appl. Phys. Lett*, **88**:204106–1–3, 2006.

[MCG02] H. Moon, S.-K. Cho, R. L. Garrel, and C.-J. Kim. "Low Voltage electrowetting-on-dielectric." *J. Appl. Phys.*, **92**:4080–4087, 2002.

[MK07] H. Moon and C.-J. Kim. "Electrowetting: Thermodynamic Foundation and Application of Microdevices." In S. Hardt and F. Schonfeld, editors, *Microfluidic Technologies for Miniaturized Analysis Systems*, chapter 5, pp. 203–236. Springer, New York, London, 2007.

[MWS99] C. D. Meinhart, S. T. Wereley, and J. G. Santiago. "PIV measurements of a microchannel flow." *Exp. in Fluids*, **27**:414–419, 1999.

[Ott89] J. M. Ottino. *The kinematics of mixing: stretching, chaos, and transport*. Cambridge University Press, Cambridge, 1989.

[Ott98] F. Otto. "Dynamics of labyrinthine pattern formation in magnetic fluids: A mean-field theory." *Arch. Rat. Mech. Anal.*, **141**:63–103, 1998.

[Peg89] R. L. Pego. "Front migration in the nonlinear Cahn Hilliard equation." *Proc. R. Soc. Lond.* A, **422**:261–278, 1989.

[PF97] A. Paterson and M. Fermigier. "Wetting on Heterogeneous surfaces: Influence of defect interactions." *Phys. Fluids*, **9**:2210–2216, 1997.

[PFL95] A. Paterson, M. Fermigier, and L. Limat. "Wetting on Heterogeneous surfaces: Experiments in an imperfect Hele-Shaw cell." *Phys. Rev. E*, **51**:1291–1298, 1995.

[PFS00] M. G. Pollack, R. B. Fair, and A. D. Shenderov. "Electrowetting-based actuation of liquid droplets for microfluidic applications." *Appl. Phys. Lett*, **77**:1725–1726, 2000.

[PH84] C.-W. Park and G. M. Homsy. "Two-phase displacement in Hele-Shaw cells: theory." *J. Fluid Mech.*, **139**:291–308, 1984.

[PMY94] C. W. Park, S. R. K. Maruvada, and D. Y. T. Yoon. "The influence of surfactants on the bubble motion in Hele-Shaw cells." *Phys. Fluids*, **6**:3267–3275, 1994.

[Pom02] Y. Pomeau. "Recent progress in the moving contact line problem: a review." *C. R. Mechanique*, **330**:207–222, 2002.

[PP04] L. M. Pismen and Y. Pomeau. "Mobility and interactions of weakly nonwetting droplets." *Phys. Fluids*, **16**:2604–2612, 2004.

[PPF03] P. Paik, V. K. Pamula, and R. B. Fair. "Electrowetting-based droplet mixers for microfluidic systems." *Lab on a Chip*, **4**:253–259, 2003.

[PQR00] V. Peykov, A. Quinn, and J. Ralston. "Electrowetting: a model for contact-angle saturation." *Colloid. Polym. Sci.*, **278**:789–793, 2000.

[PTV93] W. H. Press, S. A. Teukolsky, W. T. Vetterling, and B. P. Flannery. *Numerical Recipes in C*. Cambridge University Press, New York, second edition, 1993.

[RBH00] J. C. Rife, M. I. Bell, J. S. Horwitz, M. N. Kabler, R. C. Y. Auyeung, and W.-J. Kim. "Miniature valveless ultrasonic pumps and mixers." *Sens. Actuators A*, **86**:135–140, 2000.

[Rei87] D. A. Reinelt. "Interface conditions for two-phase displacement in Hele-Shaw cells." *J. Fluid Mech.*, **184**:219–234, 1987.

[Saf86] P. G. Saffman. "Viscous fingering in Hele-Shaw cells." *J. Fluid Mech.*, **173**:73–94, 1986.

[SDA02] A. D. Stroock, S. K. W. Dertinger, A. Ajdari, I. Mezic, H. A. Stone, and G. M. Whitesides. "Chaotic mixer for microchannels." *Science*, **295**:647–651, 2002.

[Sep96] P. Seppecher. "Moving contact lines in the Cahn-Hilliard theory." *Int. J. Engng. Sci.*, **34**:977–992, 1996.

[SH01] E. Seyrat and R. A. Hayes. "Amorphous fluoropolymers as insulators for reversible low-voltage electrowetting." *J. Appl. Phys.*, **90**:1383–1386, 2001.

[Sme03] P. Smereka. "Semi-implicit level-set method for curvature and surface diffusion motion." *J. Sci. Comp.*, **19**:439–456, 2003.

[SMG03] B. Shapiro, H. Moon, R. L. Garrel, and C.-J. Kim. "Equilibrium behavior of sessile drops under surface tension, applied external fields, and material variations." *J. Appl. Phys.*, **93**:5794–5811, 2003.

[ST59] P. G. Saffman and G. I. Taylor. "A note on the motion of bubbles in a Hele-Shaw cell and porous medium." *Q. J. Mech. Appl. Math.*, **12**:265–279, 1959.

[STI03] H. Song, J. D. Tice, and R. F. Ismagilov. "A microfluidic system for controlling reaction networks in time." *Angew. Chem., Int. Ed.*, **42**:768–772, 2003.

[SWM98] J. G. Santiago, S. T. Wereley, C. D. Meinhart, D. J. Beebe, and R. J. Adrian. "A PIV system formicrofluidics." *Exp. in Fluids*, **25**:316–319, 1998.

[Tan79] L. H. Tanner. "Spreading of silicone oil drops on horizontal surfaces." *J. Phys. D: Appl. Phys.*, **12**:1473, 1979.

[Tan86] S. Tanveer. "The effect of surface-tension on the shape of a Hele-Shaw cell bubble." *Phys. Fluids*, **29**:3537–3548, 1986.

[Tan87] S. Tanveer. "New solutions for steady bubbles in a Hele-Shaw cell." *Phys. Fluids*, **30**:651–668, 1987.

[Tan00] S. Tanveer. "Surprises in viscous fingering." *F. Fluid Mech.*, **409**:273–308, 2000.

[TS87] S. Tanveer and P. G. Saffman. "Stability of bubbles in Hele-Shaw cell." *Phys. Fluids*, **30**:2624–2635, 1987.

[TS89] S. Tanveer and P. G. Saffman. "Prediction of bubble velocity in a Hele-Shaw cell - thin-film and contact-angle effects." *Phys. Fluids* A, **1**:219–223, 1989.

[VP99] H. J. J. Verheijen and M. W. J. Prins. "Reversible electrowetting and trapping of charge: model and experiments." *Langmuir*, **15**:6616–6620, 1999.

[VR03] B. P. Vollmayr-Lee and A. D. Rutenberg. "Fast and accurate coarsening simulation with an unconditionally stable time step." *Phys. Rev.* E, **68**:066703, 2003.

[VVB99] M. Vallet, M. Vallade, and B. Berge. "Limiting phenomena for the spreading of water on polymer films by electrowetting." *Eur. Phys. J.*, **B11**:583–591, 1999.

[WB03] T. P. Witelski and M. Bowen. "ADI schemes for higher-order nonlinear diffusion equations." *Appl. Numer. Math.*, **45**:331–351, 2003.

[WBH03] B. A. Wagner, A. L. Bertozzi, and L. E. Howle. "Positive Feedback Control of Rayleigh-Benard Convection." *Discrete. Contin. Dyn. Syst. Ser. B*, **3**:619–642, 2003.

[WDU90] S. J. Weinstein, E. B. V. Dussan, and L. H. Ungar. "A theoretical study of two-phase flow through a narrow gap with a moving contact line: viscous fingerin in a Hele-Shaw cell." *J. Fluid Mech.*, **221**:53–76, 1990.

[WGM01] S. T. Wereley, L. Gui, and C. D. Meinhart. "Advanced algorithms for microscale velocimetry." *AIAA Stud. J.*, **40**:1047–1055, 2001.

[WS06] S. Walker and B. Shapiro. "Modeling the fluid dynamics of electro-wetting on dielectric (EWOD)." *J. Microelectromech. Syst.*, **15**:986–1000, 2006.

[YC06] L. Y. Yeo and C. H. Chang. "Electrowetting films on parallel line electrodes." *Phys. Rev. E*, **73**:011605–011616, 2006.

[ZB00] L. Zhornitskaya and A. L. Bertozzi. "Positivity-preserving numerical schemes for lubrication-type equations." *SIAM J. Numer. Anal.*, **37**:523–555, 2000.